OBSERVED RELATIONSHIPS BETWEEN OCEANIC KELVIN WAVES AND ATMOSPHERIC FORCING

Paul E. Roundy
And
George N. Kiladis
NOAA/CIRES Aeronomy Laboratory
Boulder Colorado

Submitted to

The Journal of Climate

May 2005

Revisions Submitted October 2005

And January 2006

Accepted January 2006

Corresponding Author Address:

Paul Roundy
NOAA/CIRES Earth System Research Laboratory, Physical Sciences Division
325 Broadway
Boulder, CO 80305

Paul.roundy@noaa.gov

Abstract

The Madden-Julian Oscillation (MJO) has been implicated as a major source of the wind stress variability that generates basin-scale Kelvin waves in the equatorial Pacific. One source of debate concerning this relationship is the apparent difference in the frequencies of the two processes.

This work utilizes data from the Tropical Atmosphere Ocean (TAO) array of moored buoys along with outgoing longwave radiation data to show by means of a multiple linear regression model and case studies that the frequency discrepancy is due to a systematic decrease in the phase speeds of the Kelvin waves and an increase in the period of the waves toward the east as conditions adjust toward El Niño. Among the potential contributing factors to this phase speed decrease is an apparent air-sea interaction that enhances the wind forcing of some of the Kelvin waves, allowing them to continue to amplify because the propagating wind stress anomaly decelerates to the speed of the developing Kelvin wave instead of the significantly faster speed of the typical MJO. Kelvin waves appear to be most effectively amplified during periods when the temperature gradient above the thermocline across the equatorial Central Pacific is strong, the thermocline shoals steeply towards the east in the Central Pacific, and/or when the phase speed of the propagating wind stress forcing is closest to that of the Kelvin wave. These conditions tend to occur as the ocean adjusts toward El Niño. Since Kelvin waves are instrumental to the development of El Niño events, isolating the detailed relationship between the waves and the MJO will lead to a better understanding of interannual ocean/atmosphere interactions.

1. **Introduction**

a. Background

Oceanic Kelvin waves are a dominant mode of variability in the equatorial Pacific (Knox and Halpern 1982; Johnson and McPhaden 1993; Cravatte et al. 2003). The apparent relationships between the Madden-Julian Oscillation (MJO, Madden and Julian 1994; Zhang 2001), oceanic Kelvin waves, and the El Niño/Southern Oscillation (ENSO) have been the subjects of much recent debate (e.g., Zhang and Gottschalck 2002). Each of these processes are characterized by different dominant frequencies, with the period of the MJO centered at around 40-50 days and Kelvin waves centered around 70 days (McPhaden and Taft 1988). Additionally, the MJO tends to propagate at about 5-7 ms^{-1} whereas the phase speeds of Kelvin waves are centered on 2-3 ms^{-1}. In spite of these differences, the dependence of Kelvin waves on the MJO is well established (Enfield 1987; McPhaden et al. 1988; Kessler et al. 1995; Kessler and Kleeman 2000; Shinoda and Hendon 2002; Kutsuwada and McPhaden 2002). This paper further examines the MJO and Kelvin waves in the context of ENSO.

It has been suggested that relationships between the MJO and Kelvin waves must be strongly nonlinear because of their differing frequencies (Lau and Shen 1988; Johnson and McPhaden 1993; McPhaden and Yu 1999; Bergman et al. 2001; Shinoda and Hendon 2002; Kutsuwada and McPhaden 2002). The nonlinear processes that couple these modes are not fully understood. Some argue that seasonal activity of the

MJO is more relevant to ENSO than are individual events (e.g., Zhang and Gottschalck 2002), possibly implying that there may not be a one-to-one relationship between the MJO and Kelvin waves, or that it may be difficult to distinguish the impact of one MJO or Kelvin wave on ENSO from that of another wave during the same period. The MJO could also force the waves through a resonance effect caused by stationary or slowly propagating patches of wind, with the most relevant forcing contributed by only the lower-frequency components of the MJO (e.g., Kessler et al. 1995; Hendon et al. 1998). However, the MJO produces much less coherent variance across neighboring wavenumbers near the 70-day band than it produces in the 40-50 day band (e.g., Madden and Julian 1994; Wheeler and Kiladis 1999; Roundy and Frank 2004a). If there exists a mechanism for the more organized 40-50 day MJO variability to force Kelvin waves, then it would likely be much more effective than any forcing by its weaker lower-frequency components in spite of any resonance effects. However, linear statistics alone would be insufficient to diagnose these processes (e.g., Roundy and Frank 2004b; 2004c). We propose a mechanism that could translate the 40-50 day forcing over the West Pacific into a lower frequency Kelvin wave in the East, diagnosed by utilizing nonlinear statistics and direct observations.

Pacific Kelvin waves tend to attain their greatest amplitudes and continuity across the entire basin during the development stages of El Niño (Kessler et al. 1995; Hendon et al. 1998; Benestad et al. 2002). The strongest westerly wind stress associated with the active MJO tends to be confined to the West Pacific during all stages of ENSO except the very warmest, when the forcing shifts to the Central Pacific (Hendon et al.

1998; Zhang and Gottschalck 2002). Although intraseasonal variability in the ocean surface and the thermocline occurs throughout the ENSO cycle, we show below that there are marked differences in the propagation characteristics of Kelvin waves that depend on the oceanic background state. This paper utilizes a multivariate statistical approach to characterize the varying relationship between the MJO and Kelvin waves. We begin with a discussion of how we apply frequency filtering to diagnose the wave signals, then we apply filtered and unfiltered data in simple preliminary analyses. Results of the preliminary analysis are give in Section 3, followed by development of the statistical model and a discussion of its implications in the context of case studies from the 1997/1998 and 2002-2003 El Niño events.

b. Detection of Kelvin Waves

The observed enhancement of Kelvin wave activity during El Niño development implies that their propagation characteristics depend on the background environment and that the Kelvin waves and ENSO may modulate each other. Johnson and McPhaden (1993) argue that Kelvin wave phase speeds vary little with the ENSO cycle. We present evidence that this portion of their analysis is incomplete, because the frequency range of their filter (59-125 day periods) caused them to exclude a crucial portion of the actual wave signal. Similarly, Cravatte et al. (2003) used the 54-98 day band. Both of these filters were designed based on an analysis of individual peaks in power spectra although the actual Kelvin wave signal is spread broadly over the spectrum in multiple discrete peaks, in part because phase accelerations and amplitude variations cause the waves to become nonsinusoidal in time. Nonsinusoidal signals require inclusion of higher-frequency harmonic components to fully resolve the part of the wave that is superimposed on the dominant waveform. The spectra shown in Figure 2 of Cravatte et al. (2003) indicate some significant power in the 30-50 day range, especially in the West and Central Pacific in Tropical Atmosphere Ocean (TAO, McPhaden 1995) 20°C isotherm depth data (lower left panel of their Figure 2), and in the east-central Pacific in TOPEX sea level height (lower right panel of their Figure 2). Some of these peaks could correspond to harmonics of 60-80 day Kelvin waves. Expanding the Kelvin wave filter to include these peaks improves the resolution of the Kelvin waves. Data filtered through the expanded band have been carefully examined for signals of other waves occurring in the higher frequency range, such as tropical instability waves (Chelton et al. 2000; Contreras 2002). These waves produce large meridional current anomalies on the equator, especially during ENSO cold periods, but our analysis suggests that their equatorial sea level and zonal current anomalies are small in comparison with anomalies generated by Kelvin waves, especially during the periods emphasized in this study. Another weakness of setting the high frequency cutoff of the filter at too low a frequency is that the direct forcing by the MJO is hard to discern unless the filter includes the dominant period range of the MJO (40-50 days). We selected the 20-day cutoff to eliminate the signals of high frequency atmospheric waves, some of which may be only weakly (if at all) related to the base Kelvin wave signal.

Lau and Shen (1988) noted a Kelvin mode in a simple model that amplifies due to the destabilization of atmospheric waves by an air-sea interaction modulated by convection and east-west temperature advection by the Kelvin wave. Lengaigne et al. (2004) describe a similar interaction mode in their more complicated model. Here, we examine observations and composites of apparent air-sea interactions that occasionally extend the forcing associated with some Kelvin waves slowly eastward, such that the waves amplify more than they would if they were forced only by the MJO without these additional effects.

2. Data

Estimates for ocean surface dynamic height, depth currents, temperature profiles, sea surface temperature (SST), and surface winds were obtained from the TAO dataset, including available data from January 1, 1988 through February, 2005. For convenience in calculating statistics, gaps in some of these datasets were filled by multiple linear regression based on observations at neighboring buoys (similar to the methodology of Kutsuwada and McPhaden (2002), except that their interpolation utilized data from different depths at the same buoy). Missing data at a given buoy was interpolated by utilizing regression relationships derived from all neighboring buoys to the north and south and to the immediate east and west. About 11 percent of the dynamic height data prior to December 1991 remained missing after the interpolation, with no missing data remaining after this date. Tests reveal that results are not sensitive to this interpolation. Outgoing longwave radiation (OLR) data were obtained from the NOAA/CDC (Liebmann and Smith 1996). Anomalies were developed from these datasets by subtracting the mean and the first three harmonics of the seasonal cycle.

Indices were next developed for Kelvin waves at all the buoys, by Fourier filtering the interpolated dynamic height anomaly time series to retain periods between 20 and 100 days. In addition to the Kelvin waves, many of these indices also include the impacts of local forcing by atmospheric disturbances (e.g., Kutsuwada and McPhaden 2002). We chose the Kelvin wave index at the equator and the dateline as a basis for analysis, because most Kelvin waves, regardless of ENSO phase, affect that region. Additionally, tropical instability waves contribute little variance there.

An index for basin-wide Kelvin wave activity was also calculated. This was obtained by calculating time series of variance of the filtered Kelvin wave indices within a 121-day centered moving window for each buoy. The Kelvin activity index is the average of these windowed variance series across all equatorial buoys from 147˚E to 110˚W.

A smooth ENSO index was developed by applying a 200-day low-pass filter to the interpolated dynamic height data and by averaging the result over the Nino 3.4 region. This dynamic height index is well correlated with the 20°C isotherm depth index of Kessler (2002). An index for the trend of ENSO was found by taking the first finite difference in time of the ENSO index. We also developed an index similar to the ENSO dynamic height index for TAO SST by the same methodology.

An index for the equatorial undercurrent (EUC) was calculated by finding the maximum eastward flow in TAO ADCP current data (e.g., Plimpton et al. 2000) for each day at depths between 75 and 200m averaged over the buoys at 140°W and 110°W. Index values are not sensitive to the depth boundaries. The resulting time series was smoothed by a 31-day centered moving average to remove high-frequency noise. This index accounts for variability of the core depth of the EUC, which is known to change with ENSO phase (e.g., Seidel and Giese 1999). An index for the average depth of the thermocline was approximated by averaging the depth of the 20°C isotherm across all equatorial buoys from 180° to 95°W (e.g., Zelle et al. 2004).

Phase speeds of positive and negative dynamic height anomalies in the 20-100 day band were measured using the slopes of trajectory lines in a Hovmoeller diagram of filtered dynamic height in comparison with similarly filtered 20°C isotherm depth data. These lines were drawn through amplitude extrema of anomalies that were continuous across the basin from 156ºE to 110ºW, using both an automated objective scheme and subjective fitting, with comparable results. Use of the filtered data simplifies the estimation, but potentially leaves out some relevant information about phase speed changes along the paths of individual anomalies, which often vary across the basin. However, this should not affect our conclusions about overall trends in phase speeds observed throughout the dataset.

3. Results

a. 2002-2003 Example

Figure 1a shows an example of the unfiltered interpolated dynamic height anomalies from the TAO array, for most of the period of the 2002-2003 El Niño (see McPhaden (2004) for a review). During the northern summer period, a series of eastward-moving disturbances consistent with downwelling (warm colors) and upwelling (cool colors) are superimposed on a general low-frequency rise in dynamic height. After a relative lull in wave activity during August through early October, high amplitude waves again occurred during mid October through December. The 20-100 day band pass filtered dynamic height are plotted in Fig. 1b to show that the filter provides a good overall fit to the principal quasi-periodic disturbances in the unfiltered data, although detailed higher or lower frequency fluctuations potentially related to the Kelvin waves are not necessarily captured. However, the filtered signal is consistent with a broad pattern of dynamic height anomalies superimposed on the long-term trends associated with the progression of the El Niño. Black lines drawn on Fig. 1b approximate the trajectories of the filtered anomalies, and are reproduced on Fig. 1a. Approximate phase speeds calculated from the trajectories are written on Fig. 1a.

Figure 2 shows the behavior of 20-100 day filtered dynamic height and total SST (Fig. 2a), 20-100 day zonal flow (Fig. 2b), total zonal current (Fig. 2c), and ocean temperature (Fig. 2d) during mid-2002 at 140°W. Taken together, the panels suggest that perturbations in the 20-100 day band are consistent with Kelvin waves propagating in and above the thermocline, because the disturbances exhibit anomalous warming and eastward flow in the crests and cooling along with westward flow in the troughs of the dynamic height anomalies. The zonal current anomalies are strongest both near the surface and in the thermocline, and they weaken below the thermocline, which is usually located at depths between 50 and 120m. The EUC is evident in Fig. 2c as the eastward flow through the period centered at around 100m. The strongest flow occurred during early June and mid July, coincident with the downwelling Kelvin waves seen in Fig. 2a-b. Westward flow is seen near the surface in the upwelling waves of early July and early September. Deep eastward flow weakened in response to the upwelling wave of late June, but then strengthened with the arrival of the July wave. After the passage of the July wave, the EUC weakened (Fig. 2c), consistent with its typical behavior during El Niño. The TAO temperature data (Fig. 2d) suggest that the July wave may have formed a front, because the temperature increased abruptly throughout the mixed layer during a sudden onset of enhanced eastward flow, although its impact on SST (Fig. 2d) was small. Other possible examples of front formation during the passage of Kelvin waves are given below in Section 2f.

b. Development of Wave and Background State Indices

Figure 3a plots the indices of low pass dynamic height, SST, and Kelvin wave activity. Local maxima in the dynamic height index tend to lead maxima in SST, and not last as long. It is obvious in Fig. 3a that Kelvin wave activity is highly episodic, and tends to be maximized during periods of high or increasing Niño 3.4 dynamic height. Periods of strongly enhanced Kelvin wave activity occur during or just prior to all ENSO warm events in the dataset, and this curve agrees well with a similarly derived measure by Hendon et al. (1998). A bar graph of approximate Kelvin wave phase speeds measured from the filtered TAO data is given in Fig. 3b, along with indices for the EUC and the Central and East Pacific thermocline depth. Kelvin wave phase speeds are plotted only when the activity index in Fig. 3a is above 60 percent of its mean value, since they are difficult to determine otherwise. It is obvious that the phase speeds vary widely, from less than 2 m/s to greater than 6 m/s (6 m/s is used as a cutoff, because faster phase speeds cannot be accurately determined). As discussed below, these surprisingly high phase speeds may be associated with Kelvin waves that are continuously forced by atmospheric disturbances moving at those speeds. It appears that Kelvin wave phase speeds have a systematic tendency to decrease over periods when there is high activity, though there are exceptions to this general pattern (e.g., an unusually fast pair of waves during mid-1997).

The EUC index averages around 1 ms^{-1}, but its strength drops off significantly during the development stages of El Niño, especially during 1992 and 1997. The period of the 1996-1998 dynamic height maximum includes two distinct periods of EUC decline. In general, the thermocline depth index indicates a shallow mean Central and East Pacific thermocline prior to El Niño development, followed by a deeper thermocline as El Niño develops, then shallow again after El Niño matures, in agreement with Kutsuwada and McPhaden (2002) and others.

c. A Simple Composite Kelvin Wave

As a basis for comparison with the statistical model developed for this study, we calculated a composite average of 20 to 100 day band pass filtered OLR, 20-100 day NCEP/NCAR Reanalysis zonal wind stress, and 20-100 day dynamic height. We first found the dates of every positive maximum of our Kelvin wave index, then averaged the filtered data over those dates (a sample size of 152) and a range of time lags. The result is shown in Fig. 4. A 40-50 day oscillation is apparent in the OLR, consistent with the MJO. Negative OLR anomalies are approximately collocated with westerly wind stress anomalies across the Indian Ocean and West Pacific. Three positive dynamic height anomalies are apparent (Fig. 4a), reflecting downwelling Kelvin waves. These are separated by two negative anomalies, or upwelling waves. Each dynamic height anomaly moves eastward more slowly than the preceding anomaly, consistent with the general trends shown in Fig. 3b. Phase speeds estimated from the dashed lines are 3.8, 2.3, and 2.1 ms^{-1}, respectively, for the three highest amplitude dynamic height anomalies from bottom to top in Fig. 3a. This pattern of deceleration is discernable in the composite because the highest amplitude waves that dominate near the lag 0 tend to be preceded by faster waves and followed by slower waves. Perhaps the most striking difference between the convectively active and suppressed phases of the MJO over the Pacific in the vicinity of the Kelvin waves is that the alternating zonal wind stress (Fig. 4b) is asymmetric in both time and longitude, with the westerly stress events concentrated in the western basin, while easterly stress anomalies move much more quickly across the basin and are most prominent east of the dateline. The same asymmetric pattern in time in the wind stress anomalies is preserved when minima of negative dynamic height anomalies are selected instead of maxima (not shown). The main weakness of this analysis is that it includes events that occur over a broad range of wave amplitudes and oceanic basic state conditions, giving the average pattern associated with the average wave. Since the details of the relationship between the Kelvin waves and the atmospheric forcing responsible for their development appear to depend strongly on the basic state, we now turn to the regression model, which allows us to focus more specifically on these periods of positive and increasing Niño 3.4 dynamic height when Kelvin waves attain their highest amplitudes.

d. A Regression Composite Kelvin Wave

Regression models based on the Kelvin wave index time series (k), the ENSO index (e), and the ENSO trend index ($\dot{e}$) were calculated to develop a more detailed composite of the Kelvin waves and the atmospheric disturbances responsible for forcing them. Unfiltered OLR anomalies, surface winds, SST, and dynamic height data were each treated as dependent variables (y). All regression models that we applied were of the form

$$\begin{aligned} y = a_0 + a_1 e + a_2 \dot{e} + a_3 k + a_4 k^2 + a_5 k^3 + a_6 k^4 + a_7 e \bullet k + a_8 \dot{e} \bullet k + \\ + a_9 e \bullet k^2 + a_{10} e \bullet k^3 + a_{11} \dot{e} k^2 + a_{12} \dot{e} k^3 + \varepsilon \end{aligned} \quad , \quad (1)$$

where the a_x coefficients are regression parameters, and ε represents the model residuals. Small but significant correlations were evident between several of the terms, so the set of predictor time series were orthogonalized in the same order that they appear in equation 1, by following the Gram/Schmidt process (Draper and Smith 1966; Press et al. 1995) as discussed by Roundy and Frank (2004c). Roundy and Frank (2004b and c) explain the utility of including the higher power terms. These terms model relationships between low-frequency predictors and higher-frequency predictands and help diagnose relationships between correlated waveforms of different shapes. The cross-product terms diagnose the effects of ENSO modulation. For example, if a given dependent variable y tends to have higher amplitudes during El Niño than during other periods, then the coefficient a_7 in (1) might be found to be positive and significantly different from zero. In that case, substitution of any value for k would then contribute to a higher amplitude value for y from this term if the value substituted for e were positive.

Equation 1 is solved by a matrix operation as discussed by Roundy and Frank (2004b). For this paper, we let e equal +1 standard deviation (SD) and $\dot{e}$ equal +2 SDs. These values typically occur during developing El Niño conditions and result in amplitudes of composite Kelvin waves and their associated forcing disturbances similar to those observed during El Niño development and were selected because of the relationship between Kelvin wave activity and the Niño 3.4 dynamic height index suggested in Fig. 3a. k was set at two SDs, corresponding to a wave crest in dynamic height at the date line and zero lag. This standard deviation of the k series was calculated only from those periods when the ENSO and ENSO trend indices were positive, because it varies significantly with ENSO phase. Statistical significance was assessed by means of a 500-iteration bootstrap test (see Appendix A of Roundy and Frank 2004b).

Though each term was included each time the model was constructed, our composites generally include only a subset of the terms. The advantage of using a subset of the model is that this allows the mean, the linear contributions of ENSO, the waves themselves, and the modulation effects to be viewed separately. Results of this analysis are considered representative because a broad set of more than 30 high-amplitude downwelling 20-100 day band Kelvin waves crossed the entire basin during this 15-year period. Our dataset includes the exceptionally strong 1997-1998 El Niño, which we suspected might dominate the statistics. We tested the importance of this event to our results by removing the period July 1996 through June 1998 from the dataset and then repeating the analysis. The structures seen in the composites were not significantly altered, but the amplitudes were slightly reduced. This implies that our composites show behavior from a variety of periods throughout the dataset.

Figure 5 shows the regression result for the linear term (term 3 only) in equation 1. Consistent with the composite averages in Fig. 4, the active MJO clearly leads to westerly wind stress and a downwelling Kelvin wave. However, the deceleration with time is much less apparent than in Fig. 4. The dashed lines from bottom to top in Fig. 5 suggest phase speeds of 3, 2.6, and 2.2 ms^{-1}, respectively. Term 3 alone can only show the portion of the actual pattern that is linearly correlated with the signal at the dateline, so it cannot diagnose all of the phase speed variability. Additionally, the asymmetry in time in the wind stress is not preserved by the linear model. In fact, switching the sign of the Kelvin wave index results in a composite structure identical to that shown in Fig. 5 with signs reversed. We show below that inclusion of the nonlinear terms in equation 1 helps to diagnose asymmetric patterns.

Figure 6 shows the longitude time lag of OLR, dynamic height (a), and zonal wind stress (b) from the regression model in equation 1. This composite assumes a strong trend towards El Niño conditions with the dynamic height anomaly of a Kelvin wave centered at the dateline and zero lag, resulting in differences between Figs. 4 and 6. Figure 6 shows just the intraseasonal component of each quantity because the background (terms 0 through 2 in equation (1)) was not included. The eastern hemisphere OLR patterns show the convective signatures of the atmospheric disturbances associated with the Kelvin waves. The lines indicate that these disturbances have eastward phase speeds between 5 and 8 ms^{-1} and periods between

40 and 50 days, matching the characteristics of the MJO. Also appearing are higher frequency signals and even some westward propagation east of the dateline. This westward propagation is the signal of atmospheric Rossby waves that are occasionally linked to the MJO (Roundy and Frank 2004 a, b). Further analysis suggests that these Rossby waves may also influence the generation of the Kelvin waves and affect a trend toward El Niño (not shown).

In Fig. 6, an initial westerly stress anomaly arrives in the TAO domain along with the eastward-moving MJO-like convective anomaly indicated by trajectory B. A portion of the OLR and stress anomalies continue eastward at about 2.1 ms^{-1} along with and behind the crest of the Kelvin wave tracked by trajectory 2 instead of at the higher speed of the composite MJO to the west of 150E. This is consistent with a similar composite of wind stress data derived from the NCEP/NCAR reanalysis (not shown), which suggests that westerlies are approximately in phase with the eastward-moving negative OLR anomaly across the eastern Indian Ocean before they decelerate to a phase speed more comparable to a Kelvin wave east of 150ºE. Successive dynamic height anomaly trajectories in Fig. 6 suggest slower propagation speeds, with trajectory 1 moving at about 2.9 ms^{-1}, trajectory 2 at about 2.1 ms^{-1}, and trajectory 3 at about 1.9 ms^{-1}. Asymmetries in the wind stress pattern similar to those seen in Fig. 4 also appear in the regression composite when different ENSO index values are substituted (such as those representing a trend away from El Niño), suggesting that these patterns change with ENSO phase (not shown).

e. Individual Cases

Case studies confirm the relationships shown in the composites including a distinct tendency for successive Kelvin waves to decelerate during periods when the Niño 3.4 dynamic height increases with time (Fig. 3b). For example, during the 1997 El Niño, the average observed phase speeds of Kelvin band (20-100 day) dynamic height anomalies decreased from over 4 ms^{-1} in November 1996 to about 2.2 ms^{-1} in August through October 1997, with the exception of an upwelling/downwelling wave pair during May-June, which were much faster.

Figure 7a shows the OLR anomalies and Fig. 7b shows OLR and Kelvin band dynamic height anomalies during 2002. As in the composite, active convection (suggested by blue shading) precedes the development of downwelling Kelvin waves, and the phase speeds of successive dynamic height anomalies progressively decrease with time as conditions trend toward El Niño. The downwelling wave at the beginning of June had a measured phase speed of about 3.8 ms^{-1}, whereas the wave during July-August was around 2.7 ms^{-1} (see also Figs. 1 and 3b). The observed deceleration results in an initial period of about 50-days in the West Pacific spreading to 70-days in the east. The relative phase speeds of the waves and anomalies of atmospheric forcing would determine the ultimate amplitude of the waves (e.g., Hendon et al. 1998). However, we show below that for some waves, the wind stress anomalies actually slow to the phase speed of the waves, allowing them to amplify across a broad region of the basin. Coupling with the atmosphere, along with other basic state effects that could influence phase speed, may also modify the wave statistics and allow for the highly variable phase speeds that we observe. We now discuss potential explanations for these results.

f. Processes Affecting Kelvin Wave Propagation

Theory predicts that several factors potentially govern the phase speed of Kelvin waves, including background currents, the depth of the thermocline, the stratification near the thermocline, nonlinear effects, wave-breaking and front formation, and the vertical structure of the Kelvin waves themselves. The phase speeds may also be modified as the waves are distorted by forcing by the atmosphere. We briefly summarize the potential contributions of each of these factors.

Of the system of currents in the equatorial region, the EUC should most affect Kelvin wave phase speed through advection because its strongest flow is located near the thermocline, where the vertical displacement associated with the waves tends to be greatest. As the trade winds weaken with El Niño onset, the EUC also weakens in response (e.g., McPhaden et al. 1986; McPhaden and Hayes 1990). In fact, flow in the EUC region was observed to switch from eastward to westward across portions of the Pacific during the 1982-1983, 1992, and 1997-1998 El Niño events (Firing et al. 1983; Seidel and Geise 1999). The decrease in EUC strength would contribute to decreasing Kelvin wave phase speeds. However, numerous theoretical and modeling studies suggest that the equatorial current system actually contributes little to Kelvin wave phase speeds (e.g., Philander 1979; Johnson and McPhaden 1993). These results have not been sufficiently tested by observations.

According to most theoretical treatments for Kelvin waves, a deeper thermocline should result in faster eastward propagation (e.g., Long and Chang 1990). Model results of Benestad et al. (2002) also suggest that a deeper thermocline, along with a stronger vertical density gradient in the thermocline, might increase Kelvin wave phase speeds during El Niño development.

In theoretical analyses, Federov and Melville (2000) suggest that nonlinear effects can increase phase speeds by 10 to 30 percent in regions where the thermocline is shallow or shoaling. Their model also indicates that wave breaking in response to a sharply shoaling thermocline might result in even faster eastward-propagation of downwelling Kelvin waves. Kelvin waves in their analysis are internal waves that are initially confined to propagate along a strong nearly vertical density gradient of the thermocline. These Kelvin waves may be forced to propagate vertically and break when the isopycnals shoal steeply eastward. The waves then form fronts or hydraulic jumps, which propagate eastward at a higher speed than that of linear waves. These fronts abruptly advect mixed layer isotherms eastward, allowing the waves to subsequently increase the SST to the east. In contrast, waves in their model that do not contain fronts propagate parallel to lines of constant density. Such waves would still produce temperature anomalies by raising or lowering the thermocline. Because nonlinear effects and wave breaking are more likely to contribute to higher phase speeds early in El Niño development when the thermocline shoals more steeply toward the east, a reduced dependence on these factors might result in decreased phase speeds as El Niño matures.

Observed changes in Kelvin wave phase speeds may also be associated with changes in the dominance of higher baroclinic modes (e.g., Giese and Harrison 1990; Benestad et al. 2002; Cravatte et al. 2003; and others). Since they are forced from the surface, these higher modes propagate energy downward and have upward phase propagation. These waves also propagate more slowly than barotropic and first baroclinic mode waves. It is possible that part of the decrease in observed phase speeds during periods of El Niño development could be associated with a tendency for the earlier waves to be dominated by first baroclinic mode structures while the later waves may be dominated by the second or higher mode structure (Dewitte et al. 2003).

We can only speculate about the actual causes of the observed frequency spreading due to both a lack of adequate data and because covariation between the relevant parameters make it difficult to sort out cause and effect. Figure 3b does indicate that the EUC weakens with time as conditions trend toward El Niño, but the decrease in advection by the current is not sufficient to explain the total decrease in observed phase speeds unless the effects are somehow amplified by nonlinearity. Figure 3b also suggests that the depth of the thermocline decreases across most of the basin after El Niño matures, which might reduce phase speeds then, but the relationship is noisy. The mechanism of Kelvin wave phase speed change is currently being investigated using the Hybrid Coordinate Ocean model (HYCOM, Bleck 2002). Our preliminary results indicate that the model is able to reproduce the phase speeds of the fast waves observed during the 2002 period only when the model ocean was continuously forced by observed winds. In the absence of continued forcing, the fast waves move at the first baroclinic mode phase speed, suggesting that forcing generated by atmospheric waves is largely responsible for the high phase speeds (T. Shinoda, personal communication). It is unlikely that any one of these potential factors acts alone in controlling the observed phase speed variability. Regardless of the cause(s) there is strong evidence throughout the available data that Kelvin wave phase speeds tend to decrease with time during periods of increasing low frequency dynamic height.

Our results suggest that the observed 70-day period of the Kelvin waves may not entirely result from rectification of the wind stress or from just the low-frequency tail of the MJO, as speculated by Kessler and Kleeman (2000), Zhang and Gottschalck (2002), and others. It also may not necessarily result from some preferred frequency characteristic of the waves themselves. Instead, decreases in the phase speeds of the waves over the course of a trend towards El Niño appear to contribute substantially to their observed reduced frequency in the eastern Pacific. These observations show that Kelvin waves simply tend to take longer to cross the central and eastern Pacific as El Niño matures than they take during its initial development stage.

g. Amplification of Kelvin Waves By Air-Sea Interaction

Figure 6 shows that during a trend toward El Niño, the phase speed of the OLR propagation approaches that of the Kelvin waves to the east of 150°E, suggesting ocean-atmosphere coupling. We now discuss several potential cases of air-sea interactions modifying the relationships between convection, wind stress, and SST, followed by a more detailed analysis of the regression composite.

The OLR and dynamic height patterns shown in Fig. 7a suggest that atmospheric convection responds to the oceanic waves. Portions of the eastward-propagating OLR anomalies seen in early May (Event A) and mid-June (Event B) slow down and propagate close to the trajectories of the downwelling Kelvin waves. Figures 8 and 9 show anomalous 20-100 day and total SST, respectively, during northern summer 2002. These figures show that the May-June wave dramatically increased SST along its trajectory. Zonal current anomalies of this wave advected warm water eastward across the strong background temperature gradient suggested in Fig. 9. The temperature increase associated with this wave occurred at the leading edge of both the dynamic height and current anomalies, consistent with zonal advection. TAO zonal wind data (not shown) indicate that a westerly anomaly greater than 3 ms^{-1} preceded the crest of the May-June wave all the way to 150°W. The dynamic height anomaly amplified until it reached about 140°W (e.g., Fig. 8).

In contrast, the July wave exhibited a stronger eastward-flow anomaly below the surface (Fig. 2b and c), but was associated with weaker wind and SST anomalies east of the dateline (winds not shown, SST shown in Fig. 8). Though the initial zonal wind anomaly that triggered the July wave exceeded 8 ms^{-1} near 150°E, it weakened dramatically to below 3 ms^{-1} near the dateline and diminished eastward. In comparison with the earlier wave, the July wave exhibited higher amplitude dynamic height anomalies in the West Pacific and lower amplitude farther east, consistent with the observed winds. The more strongly enhanced background convection early in the path of the July wave may have reduced the rate of SST increase from eastward advection, thereby weakening the response of the winds. In any case, this result may suggest that the atmospheric response to the waves depends on the magnitude of the SST anomalies that they produce.

Other examples of air-sea interactions associated with apparent Kelvin wave fronts were observed during 1997. Figure 10 shows the dynamic height, currents, and temperatures for January through mid-September 1997 at 140°W. A temperature jump of greater than two degrees (near 100m depth) occurred in less than four days around March 18 as the eastward flow anomaly of a downwelling wave developed. Isotherms were nearly vertical during March, 1997, (e.g., Figure 1 of Federov and Melville 2000), and would have supported front formation. Figure 10 suggests that similar temperature increases occurred with downwelling waves of June and August.

The equatorial OLR patterns associated with the MJO events that were responsible for triggering the downwelling waves of June and July-August are shown in Fig. 11. The OLR anomaly labeled 1 in Fig. 11 shows a distinct deceleration as the June wave developed, and the anomaly labeled 2 shows an even more pronounced deceleration as the July wave developed. Figure 12 shows the OLR and 11-100 day band SST anomalies for the period of trajectory 2 in Fig. 11. Positive 20-100 day band dynamic height anomalies are included for reference. The dynamic height anomaly is collocated with a positive SST anomaly, which is followed roughly 10° to the west by the minimum in OLR, which in turn is followed by a negative SST anomaly (presumably generated by the cooling effects of the convection).

These observations suggest different patterns of air-sea coupling with different waves. Nevertheless, the composite suggests relationships between convection, wind, and SST during a trend toward El Niño. Figure 13 maps the structures of the regressed OLR, wind, dynamic height, and total anomalous SST associated with the downwelling wave along trajectory 2 in Fig. 6. Active convection associated with the MJO is in the far western basin at a lag of -18 days in Fig. 13a. Subsequent panels of Fig. 13 show the negative OLR anomalies becoming distributed across much of the basin. Some of these OLR anomalies occur in a pattern with respect to the SST anomalies that appears to be consistent with a particular type of air-sea coupling. Initially, a positive SST anomaly leads the crest of the Kelvin wave and an OLR minimum (the OLR minimum is labeled A in Fig. 13 b-e). A westerly wind anomaly blows through the active convection toward the positive SST anomaly, and the Kelvin wave dynamic height anomaly amplifies and propagates eastward. The SST anomaly expands eastward more slowly than the dynamic height anomaly propagates, so that they become collocated at lag 0 (Fig. 13 d). The equatorial SST anomaly maximum is followed by OLR anomaly A between 10 and 20 degrees to the west. This OLR minimum is absorbed into a broader OLR minimum to the east and south around lag +10 to +12 days (Fig. 13f). After lag +12 days, the dynamic height anomaly reaches its maximum, the wind forcing behind the wave crest decreases, the remnant OLR anomaly weakens and shifts into the southern hemisphere, and the SST anomaly expands across the basin.

The patterns in Figs. 12 and 13 differ from those typically associated with the MJO. Over the Indian Ocean and West Pacific, large-scale SST anomalies are generally in quadrature with MJO OLR anomalies (e.g., Jones et al. 1998; Shinoda et al. 1998). Figures 12 and 13 suggest that when the MJO couples to a Kelvin wave, the highest SSTs may be closer to the active convection than in an MJO farther west, and the zonal scales of anomalies are reduced. The ocean-atmosphere coupling occurs in a manner that slows the eastward progression of the convection initially associated with the MJO, and probably enhances the amplification of the Kelvin waves by extending the duration of the forcing west of the Kelvin wave crest.

This air-sea interaction appears to allow some Kelvin waves to sustain their own continued growth by means of their advective SST anomalies interacting with convection and winds. This behavior during El Niño development is sometimes similar to that of the theoretical “advective mode” discussed by Lau and Shen (1988), and to the interaction discussed by Lengaigne et al. (2004). Figure 12 and Fig. 13 (panels b-e) suggest convection lagging west of SST and dynamic height by roughly 10° longitude, consistent with the advective mode during periods when coupling is apparent. Interestingly, this advective mode predicts phase speed to decrease with time as the zonal mean SST increases and the zonal SST gradient weakens, such as occurs during a trend toward El Niño.

This coupled interaction is often clearly discernable in individual cases, especially during periods when the highest background SSTs are moving into the Central Pacific during the first stages of El Niño development, but it does not occur in the same way during every Kelvin wave. For example, during the earliest stages of El Niño development, the atmospheric forcing does not slow down as much and results in surprisingly fast oceanic disturbances (e.g., the May 2002 events, which moved faster than 4-5 ms^{-1}). Conversely, during more mature El Niño conditions, Kelvin waves and their associated forcing tend to move surprisingly slowly (e.g., about 1.5 ms^{-1} during January 2002). Other waves do not follow the general pattern of phase speed decrease during a trend toward El Niño (e.g., the fast wave of June 1997).

Eastward temperature advection by Kelvin waves becomes less effective after El Niño matures because of the relaxation of the zonal temperature gradient (as discussed by Bergman et al. 2001). Eastward advection of temperature may be necessary to produce the SST anomalies that facilitate the interactions, so the wave amplification likely occurs preferentially when the zonal SST gradient is strong in the Central Pacific. Only downwelling Kelvin waves form fronts under these conditions, allowing eastward advection to contribute significantly to the temperature anomalies the waves produce, whereas upwelling waves are largely limited to affecting temperature through raising the thermocline (Federov and Melville 2000). This asymmetry about Kelvin wave phase is probably responsible for at least a portion of the asymmetry in the wind stress patterns seen in Figs. 4 and 6, because air-sea coupling behaves differently in waves dominated by zonal advection than in waves dominated by upwelling (e.g., Lau and Shen 1988).

4. Conclusions

An analysis of TAO buoy and OLR data indicates that one source of the frequency difference between the MJO and oceanic Kelvin waves is a transient decrease in Kelvin wave phase speeds as oceanic conditions tend toward El Niño. The slower phase speeds delay the arrival of subsequent Kelvin waves into the East Pacific, thus reducing their frequency as the background conditions change. It is also suggested that an air-sea interaction occasionally enhances and extends the MJO-induced wind-stress forcing of Kelvin waves as El Niño develops. After the initial triggering of the Kelvin wave by the MJO westerlies, the eastward flow anomalies of the Kelvin wave then advect warm water eastward. Convective and wind stress anomalies respond by slowing down to the phase speed of the waves. This suggests a form of air-sea coupling that is sometimes similar to that of the advective mode of Lau and Shen (1988). The eastward phase speed of this theoretical coupled mode decreases with time as conditions trend toward El Niño, consistent with our observations. Our results indicate that not only is the effective fetch of the MJO-induced wind stress patch increased during El Niño development (as suggested by Kessler et al. 1995), but the eastward propagation speed of the effective forcing is often reduced as well, resulting in even further enhancement of the wave amplification process. This reduction in the phase speed of the wind stress anomalies is less likely to occur in association with upwelling waves than in downwelling waves (e.g., Figs. 4 and 6), suggesting that the air-sea coupling favors downwelling waves.

Our conclusions differ from those of Benestad et al. (2002), who suggest that Kelvin waves should accelerate during El Niño because of increased thermocline depth in the Central and East Pacific and other factors (see their Figure 5). The impacts of the air-sea interactions that occur in the real ocean atmosphere system are presumably still present in the atmospheric data that they use to force their model. Nevertheless, if the speeds of the simulated Kelvin waves are not sufficiently close to the observed speeds, the wind forcing may not be phased appropriately to the waves. This is likely a very sensitive result that depends on the ocean model used.

Kelvin waves become most active during a trend toward mature El Niño conditions, but such conditions apparently lead to weakening of the Kelvin wave generation process, because the strongest coupling occurs when the zonal temperature gradient is strong enough for advection across it to produce significant positive SST anomalies (Hendon et al. 1999; Bergman et al. 2001; Lengaigne et al. 2004). Our continued research will focus on how the relationships between the forcing modes and the Kelvin waves change with the background state, including different phases of ENSO.

Acknowledgements

Funding for this work was provided by the NOAA office of Global Programs under grant GC01-351 to GNK. The TAO Project Office of NOAA/PMEL provided the mooring time series data. Four anomymous reviewers offered valuable feedback on this and earlier versions of the manuscript. Stimulating conversations with Pat Haertel, Harry Hendon, Billy Kessler, Mike McPhaden, Dennis Moore, Toshi Shinoda, Klaus Weickmann, and Chidong Zhang were helpful to clarify several of the ideas in this study.

References

Benestad, R. E., R. T. Sutton, and D. L. T. Anderson, 2002: The effect of El Niño on intraseasonal Kelvin waves. *Q. J. R. Meteorol. Soc.*, **128**, 1277-1291.

Bergman, J.W., H.H. Hendon, and K.M. Weickmann, 2001: Intraseasonal air-sea interactions at the onset of El Niño. *J. Climate*, **14**, 1702-1718.

Bleck, R., 2002: An oceanic general circulation model framed in hybrid isopycnic-cartesian coordinates. *Ocean Modelling*, **4**, 55-88.

Chelton, D.B., F.J. Wentz, C.L. Gentman, R.A. DeSzoeke, and M.G. Schlax, 2000: Satellite microwave SST observations of transequatorial tropical instability waves. *Geophys. Res. Lett.*, **27**, 1239-1242.

Contreras, R. F., 2002: Long-term observations of tropical instability waves. *J. Phys. Oceanog.* **32**, 2715-2722.

Cravatte, S., J. Picaut, and G. Eldin, 2003: Second and first baroclinic Kelvin modes in the equatorial Pacific at intraseasonal time scales. *J. Geophys. Res.* **108**, 22: 1-20.

Dewitte B., S. Illig, L. Parent, Y. duPenhoat, L. Gourdeau, and J. Verron, 2003: Tropical Pacific baroclinic mode contribution and associated long waves for the 1994–1999 period from an assimilation experiment with altimetric data, *J. Geophys. Res.*, **108**, 3121, doi:10.1029/2002JC001362.

Draper, N.R., and H. Smith, 1966: *Applied Regression Analysis*. John Wiley & Sons, Inc.

Enfield, D.B., 1987: The intraseasonal oscillation in eastern Pacific sea levels: How is it forced*? J. Phys. Oceanogr.*, **17**, 1860-1876.

Fedorov, A.V., and W.K. Melville, 2000: Kelvin fronts on the equatorial thermocline. *J. Phys. Oceanog.*, **30**, 1692-1705.

Firing, E., R. Lukas, J. Sadler, and K. Wyrtki, 1983: Equatorial undercurrent disappears during 1982-1983 El Niño. *Science*, **226**, 1069-1071.

Giese, B. S., and D. E. Harrison, 1990: Aspects of the Kelvin wave response to episodic wind forcing. *J. Geophys. Res.*, **95**, 7289-7312.

Hayes, S. P., M. J. McPhaden, and J. M. Wallace, 1989: The influence of sea-surface temperature on surface wind in the eastern equatorial Pacific: Weekly to monthly variability. *J. Climate*., **2**, 1500—1506.

Hendon, H.H., B. Liebmann, and J. D. Glick, 1998: Oceanic Kelvin waves and the Madden-Julian Oscillation. *J. Atmos. Sci.*, **55**, 88-101.

Hendon, H. H., and M. L. Salby, 1994: The life cycle of the Madden-Julian Oscillation. *J. Atmos. Sci.*, **51**, 2225-2237.

Johnson, E. S., and M. J. McPhaden, 1993: Structure of intraseasonal Kelvin waves in the equatorial Pacific Ocean. *J. Phys. Oceanogr.*, **23**, 608-625.

Jones, C., D. E. Waliser, and C. Gautier, 1998: The influence of the Madden-Julian oscillation on ocean surface heat fluxes and sea surface temperature. *J. Climate*, **11**, 1057-1072.

Kessler, W. S., 2001: EOF representations of the Madden-Julian Oscillation and its connection with ENSO. *J. Climate*, **14**, 3055-3061.

Kessler, W. S., 2002: Is ENSO a cycle or a series of events? J. Geophys. Res., 29, 40-4.

Kessler, W. S., M. J. McPhaden, and K. M. Weickmann, 1995: Forcing of intraseasonal Kelvin waves in the equatorial Pacific. *J. Geophys. Res.*, **100**(C6), 10613-10631.

Kessler, W. S., and R. Kleeman, 2000: Rectification of the Madden-Julian Oscillation into the ENSO cycle. *J. Climate*, **13**, 3560-3575.

Knox, R. A. and D. Halpern, 1982: Long range Kelvin wave propagation of transport variations in Pacific Ocean equatorial currents. *J. Mar. Res.*, **40**, suppl., 329-339.

Kutsuwada, K., and M. McPhaden, 2002: Intraseasonal variations in the upper equatorial Pacific Ocean prior to and during the 1997-1998 El Niño. *J. Phys. Oceanogr.*, **32**, 1133-1149.

Lau, K.-M., and S. Shen, 1988: On the dynamics of intraseasonal oscillations and ENSO. *J. Atmos. Sci.*, **45**, 1781-1797.

Lengaigne, M., E. Guilyardi, J. P. Boulanger, C. Menkes, P. Delecluse, P. Innes, J. Cole, and J. Slingo, 2004: Triggering of El Niño by westerly wind events in a coupled general circulation model. *Climate Dynamics*, 10.1007/s00382-004-457-2.

Liebmann, B., and C. A. Smith, 1996: Description of a complete (interpolated) outgoing longwave radiation dataset. *Bull. Amer. Meteor. Soc.* **77**, 1275-1277.

Long, B., and P. Chang, 1990: Propagation of an equatorial Kelvin wave in a varying thermocline. *J. Phys. Oceanog.*, **20**, 1826-1841.

Madden, R. A., and P. R. Julian, 1994: Observations of the 40-50-day tropical oscillation-A review. *Mon. Wea. Rev.*, **122**, 814-837.

McPhaden, M. J., 1995: TAO array is completed. *Bull. Amer. Meteor. Soc.*, **76**, 739-741.

McPhaden, M. J., 2004: Evolution of the 2002/2003 El Niño. *Bull. Amer. Meteor. Soc.,* **85**, 677-695.

McPhaden, M. J., H. P. Freitag, S.P. Hayes, and B.A. Taft, 1988: The response of the equatorial Pacific Ocean to a westerly wind burst in May 1986. *J. Geophys. Res.*, **93**, 10589-10603.

McPhaden, J. J., and S. P. Hayes, 1990: Variability in the eastern equatorial Pacific Ocean during 1986-1988. *J. Geophys. Res.*, **95**, 13195-13208.

McPhaden, M. J., and B. A. Taft, 1988: On the dynamics of seasonal and intraseasonal variability in the eastern equatorial Pacific. *J. Phys. Oceanogr.*, **18**, 1713-1732.

McPhaden, M. J., J. A. Proehl, and L.M. Rothstein, 1986: The interaction of equatorial Kelvin waves with realistically sheared zonal currents. *J. Phys. Oceanog.,* **16**, 1499-1515.

McPhaden, M. J., and X. Yu, 1999: Equatorial waves and the 1997-1998 El Niño. *Geoph. Res. Let.*, **26**, 2961-2964.

Philander, S. G. H., 1979: Equatorial waves in the presence of the equatorial undercurrent. *J. Phys. Oceanog.*, **9**, 254-262.

Plimpton, P. E., H. P. Freitag, and M. J. McPhaden, 2000: Correcting moored ADCP data for fish-bias errors at 0°, 110°W and 0°., 140°W from 1993 to 1995. NOAA Tech. Memo. ERL PMEL-111, 17pp.

Press, W. H., S. A. Teukolsky, W.T. Vetterling, and B.P. Flannery, 1995: *Numerical Recipes in C: The Art of Scientific Computing*, 2nd Edn. Cambridge University Press, Cambridge, UK.

Roundy, P. E., and W. M. Frank, 2004a: A climatology of waves in the equatorial region. *J. Atmos. Sci.*, **61**, 2105-2132.

Roundy, P. E., and W. M. Frank, 2004b: Effects of low-frequency wave interactions on intraseasonal oscillations. *J. Atmos. Sci.*, 61, 3025-3040.

Roundy, P. E., and W. M. Frank, 2004c: Applications of a multiple linear regression model to the analysis of relationships between eastward-and westward-moving intraseasonal modes. *J. Atmos. Sci.*, **61**, 3041-3048.

Seidel, H. F., and B. S. Giese, 1999: Equatorial currents in the Pacific Ocean 1992-1997. *J. Geophys. Res.*, **104**, 7849-7863.

Shinoda, T. and H. H. Hendon, 2002: Rectified wind forcing and latent heat flux produced by the Madden-Julian Oscillation. *J. Climate*, **15**, 3500-3507.

Wheeler, M., G. N. Kiladis, and P. J. Webster, 2000: Large-scale dynamical fields associated with convectively coupled equatorial waves. *J. Atmos. Sci.*, **57** 613-640.

Zelle, H., G. Appeldoorn, G. Burgers, and G.J. van Oldenborgh, 2004: The relationship between sea surface temperature and the thermocline depth in the eastern equatorial Pacific. *J. Phys. Oceanog.*, **34**, 643-655.

Zhang, C. D., 2001: Intraseasonal perturbations in sea surface temperatures of the equatorial eastern Pacific and their association with the Madden-Julian oscillation, *J. Climate*, **14**, 1309-1322.

Zhang, C., and J. Gottschalck, 2002: SST anomalies of ENSO and the Madden-Julian Oscillation in the equatorial Pacific. *J. Climate*, **15**, 2429-2445.

Zhang, C., H.H. Hendon, W.S. Kessler, and A. Rosati, 2001: A workshop on the MJO and ENSO. *Bull. Ameri. Metero. Soc.*, **82**, 971-976.

Figure Captions

Figure 1 Longitude-time diagrams of unfiltered (panel a) and 20-100 day filtered dynamic height anomalies (panel b) during mid-2002 through early 2003 at the equator. The contour interval in panel b is 2 cm and the zero contour is omitted. Black lines are approximate trajectories of the filtered anomalies, and the corresponding phase speeds are shown in panel a. Trajectories are drawn only on those anomalies that include a third contour. Longitude tick marks are at buoy locations.

Figure 2 Time series and time-depth cross sections from 1 May through 10 September 2002. a. Time series of 20-100 day filtered dynamic height and total SST at the equator, 140°W (cm). b. Time-depth cross-section of 20-100 day band zonal current anomalies (cms^{-1}) from uninterpolated ADCP data. c. Total current corresponding to the anomalies in b. d. Unfiltered temperature °C. Missing data are not plotted.

Figure 3 a. Time series of Nino 3.4 dynamic height (shown in red) and SST (°Cx10, shown in green), and the Kelvin wave activity index (cm^2, black) from 1988 through September 2003. b. Phase speeds of anomalies of dynamic height in the 20-100 day band (ms^{-1}, bars), the index of the EUC (ms^{-1}, red), and the index of the thermocline depth (m, light blue). The axis label for the phase speeds is given on the left, and the EUC and thermocline depth labels are given on the right.

Figure 4 Composite average OLR (shading in a and b, with the darkest blue suggesting -17 Wm^{-2} and the red suggesting about +17 Wm^{-2}), 20-100 day dynamic height (contours in panel a), and 20-100 day NCEP reanalysis wind stress (m^2s^2, westerly contoured in red, easterly in blue), and dynamic height. Wind stress contours are included every 1 m^2s^{-2}, with the zero line omitted. Dynamic height contours are plotted every quarter cm, with the zero line omitted. Positive dynamic height contours are black with a yellow highlight, and negative anomalies are contoured with a dash-dotted line and a green highlight. The heavy dashed lines represent approximate trajectories of dynamic height anomalies. OLR is averaged from 10ºS to 10ºN, wind stress is averaged from 5ºS to 5ºN, and dynamic height is at the equator.

Figure 5 Fully linear regression composite of OLR, TAO wind stress, and dynamic height, including only term 3 in equation 1, contoured as in Figure 4. The wind stress contour interval is 3 m^2s^{-2}, with minimum contours at +/- 1.5 m^2s^{-2}. Dynamic height contours are drawn every 1 cm, with the zero line omitted. Quantities are averaged in latitude as in Fig. 4.

Figure 6 Longitude-time lag regression composite of OLR, the zonal component of the TAO wind stress, and dynamic height, plotted as described in Figures 5, except that panel a shows regressed OLR and dynamic height and panel b shows OLR and wind stress. This composite is based on an index of Kelvin wave dynamic height at the equator and the dateline, and includes terms in equation 1 with subscripts 3-12. Solid lines labeled a-d track active and suppressed phases of the MJO, while dashed trajectory lines (labeled 1-4) track Kelvin wave dynamic height anomalies. Quantities are averaged in latitude as in Fig. 4.

Figure 7 OLR and dynamic height anomalies during 2002. Panel a shows OLR only, for clarity. Dynamic height anomalies were band pass filtered for the 20-100 day periods, and negative anomalies are dashed and positive are solid. Contours are every 2 cm, except that the zero contour is removed. Trajectories of prominent eastward moving negative OLR anomalies are traced by heavy solid lines in panel a.

Figure 8 20-100 day band pass filtered dynamic height and SST on the equator preceding the 2002 El Niño, for the same period shown in Figures 2 and 7. Thick gray contours represent negative dynamic height anomalies and black positive anomalies. Dashed contours represent negative SST anomalies and shading represents positive SST anomalies. Contour intervals are 2cm (with the zero contour omitted) and 0.25°C.

Figure 9 Total SST on the equator for the development period of the 2002 El Niño. Heavy solid lines approximate the trajectories of the dynamic height anomalies of the two downwelling Kelvin waves seen in the first half of Figure 1 and in Figures 2, 7, and 9. Contour interval is 0.5°C.

Figure 10 As in Figure 2, except for 23 December 1996 through 20 September 1997.

Figure 11 Total OLR (shaded) and 20-100 day band dynamic height (both on the equator). Contour interval for the dynamic height is 1 cm, and negative contours are not plotted. White lines approximate trajectories of strong negative OLR anomalies.

Figure 12 OLR anomaly (shading), SST (positive shown in red contours, negative in blue), and positive dynamic height contours (thin black contours), for the event labeled trajectory 2 in Figure 12. SST contours are every 0.1°C, and the zero contour is omitted. All quantities are plotted on the equator.

Figure 13 Maps of regressed OLR anomaly (shading), dynamic height (green contours in integer cm, contours beginning at 2 cm), positive SST anomalies (red contours, at intervals of 0.25°C), and TAO surface winds (vectors) for lags of –24 to 6 days wind an interval of 6 days. The regressed SST data includes the ENSO modulation terms (1 and 2 in equation 1) in addition to the intraseasonal terms 3-12 that are included in the dynamic height and wind composites. The largest vectors are around 3 ms^{-1}.

Figure 1

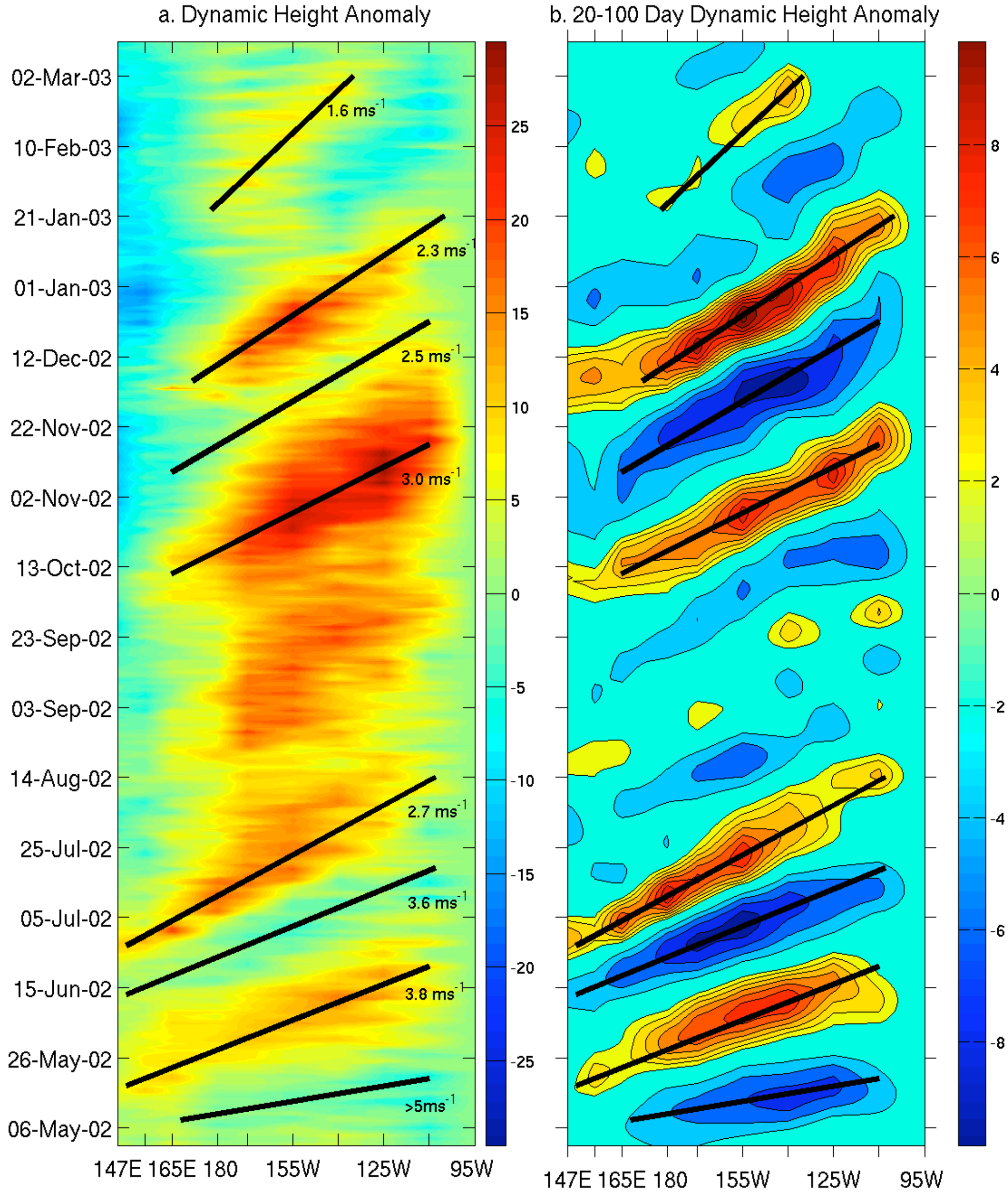

Figure 1 Longitude-time diagrams of unfiltered (panel a) and 20-100 day filtered dynamic height anomalies (panel b) during mid-2002 through early 2003 at the equator. The contour interval in panel b is 2 cm and the zero contour is omitted. Black lines are approximate trajectories of the filtered anomalies, and the corresponding phase speeds are shown in panel a. Trajectories are drawn only on those anomalies that include a third contour. Longitude tick marks are at buoy locations.

Figure 2

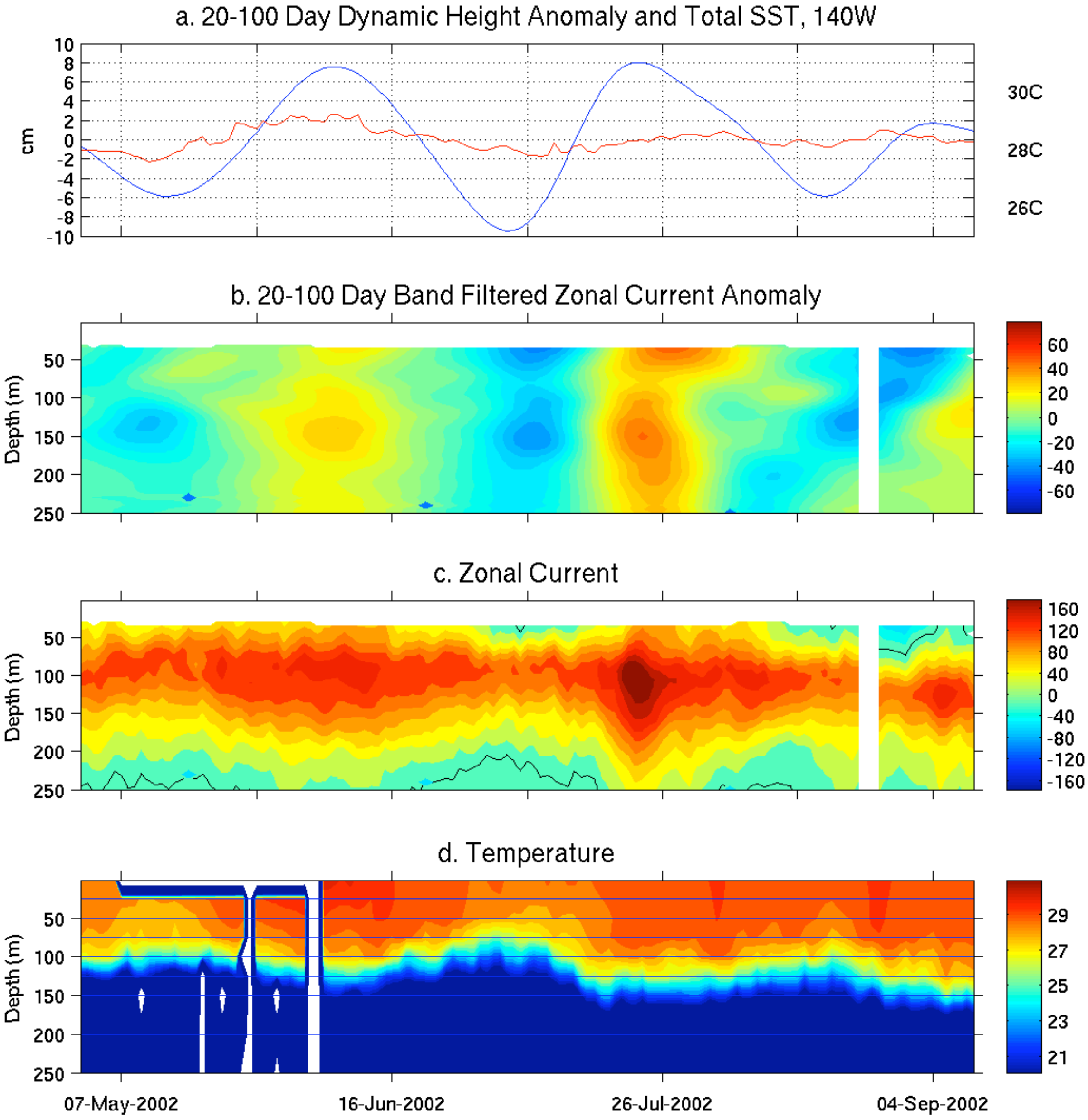

Figure 2 Time series and time-depth cross sections from 1 May through 10 September 2002. a. Time series of 20-100 day filtered dynamic height and total SST at the equator, 140°W (cm). b. Time-depth cross-section of 20-100 day band zonal current anomalies (cms-1) from uninterpolated ADCP data. c. Total current corresponding to the anomalies in b. d. Unfiltered temperature °C. Missing data are not plotted.

Figure 3

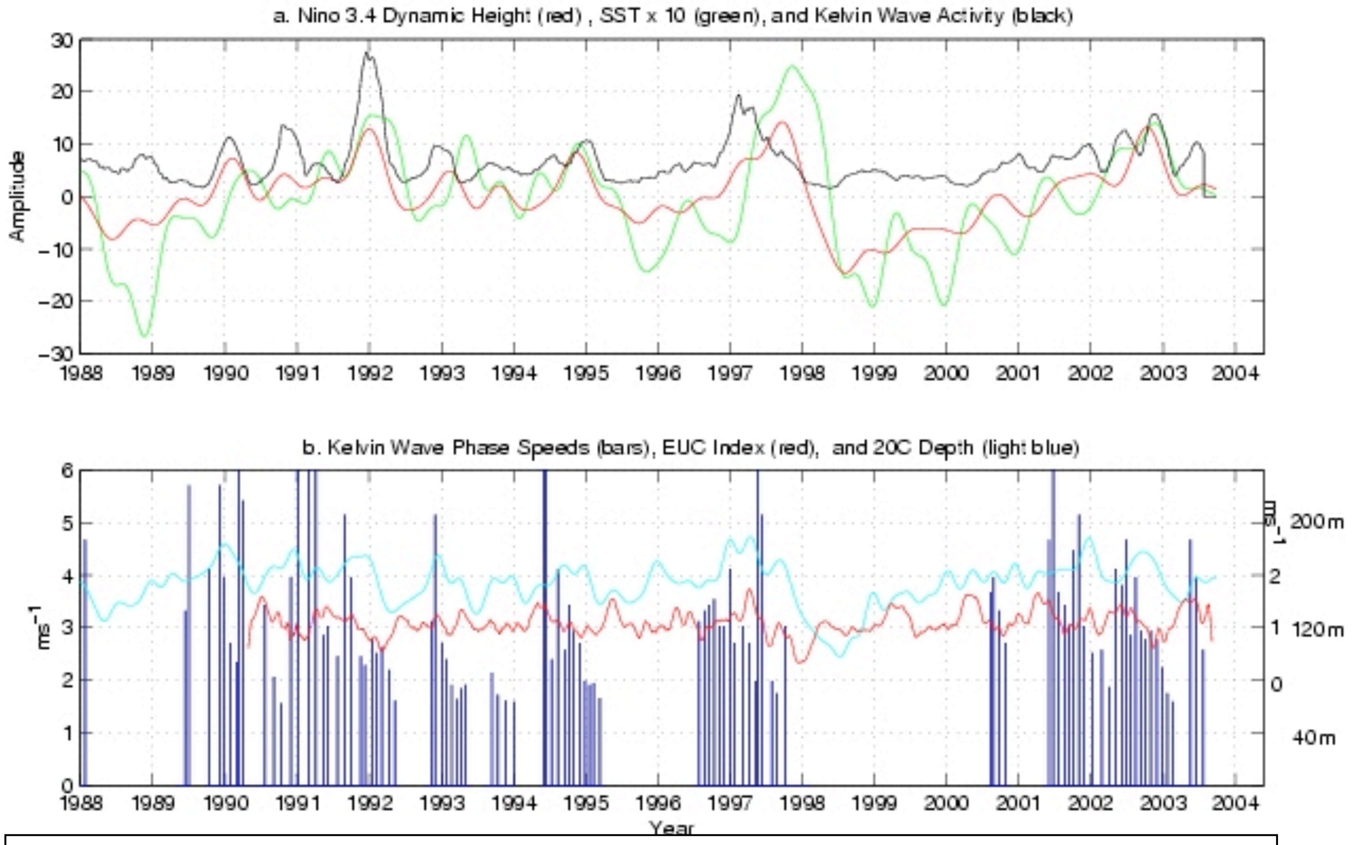

Figure 3 a. Time series index of the Nino 3.4 dynamic height (shown in red) and SST (°Cx10, shown in green) indices, and the index of Kelvin wave activity (cm^2, black) from 1988 through September 2003. b. Phase speeds of anomalies of dynamic height in the 20-100 day band (ms^{-1}, bars), the index of the EUC (ms^{-1}, red), and the index of the thermocline depth (m, light blue). The axis label for the phase speeds is given on the left, and those for the EUC and thermocline depth are given on the right.

Figure 4

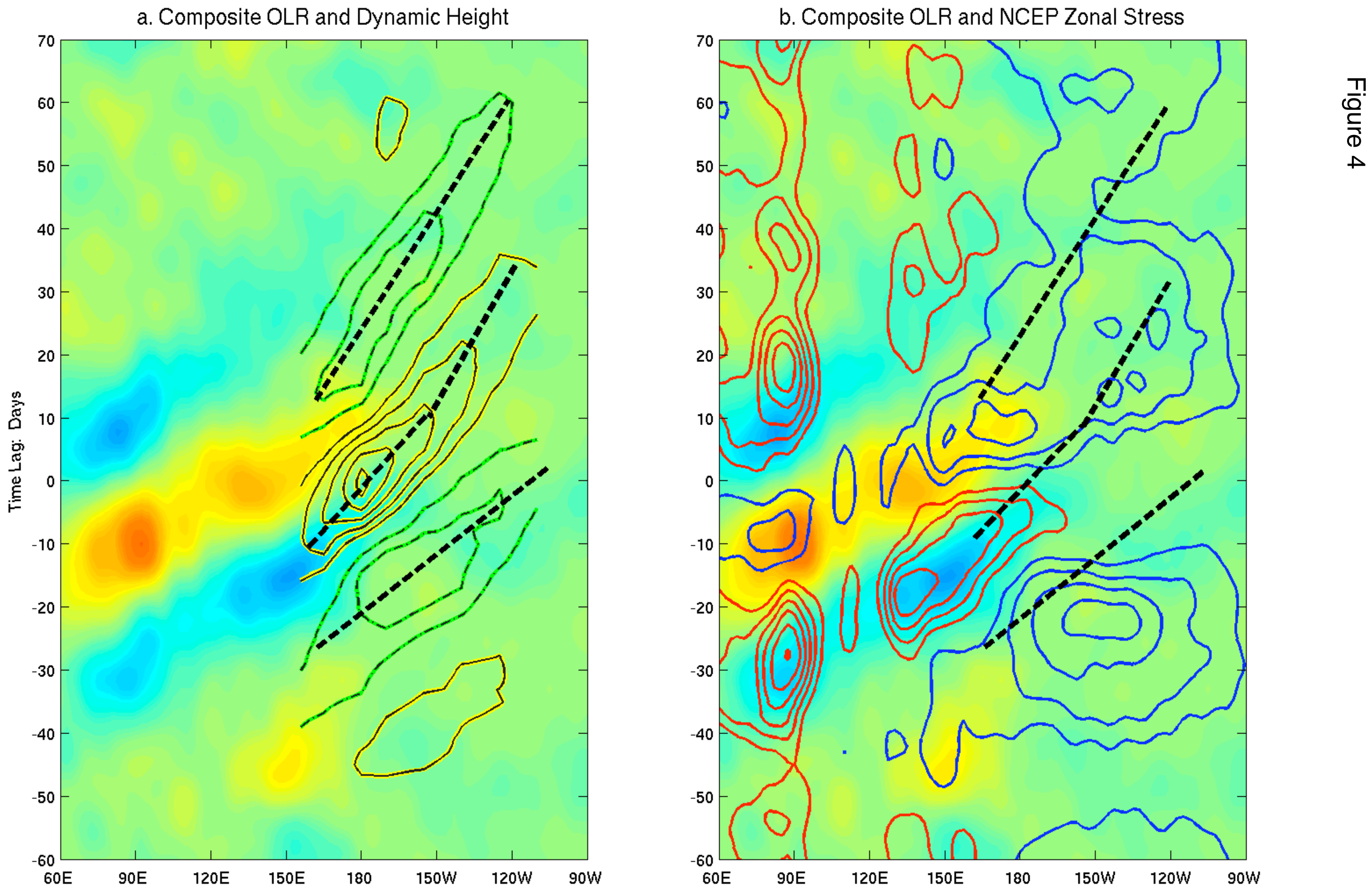

Figure 4 Composite average OLR (shading in a and b, with the darkest blue suggesting -17 Wm^{-2} and the red suggesting about +17 Wm^{-2}), 20-100 day dynamic height (contours in panel a), and 20-100 day NCEP reanalysis wind stress (m^2s^2, westerly contoured in red, easterly in blue), and dynamic height. Wind stress contours are included every 1 m^2s^{-2}, with the zero line omitted. Dynamic height contours are plotted every quarter cm, with the zero line omitted. Positive dynamic height contours are black with a yellow highlight, and negative anomalies are contoured with a dash-dotted line and a green highlight. The heavy dashed lines represent approximate trajectories of dynamic height anomalies. OLR is averaged from 10°S to 10°N, wind stress is averaged from 5°S to 5°N, and dynamic height is at the equator.

Figure 5

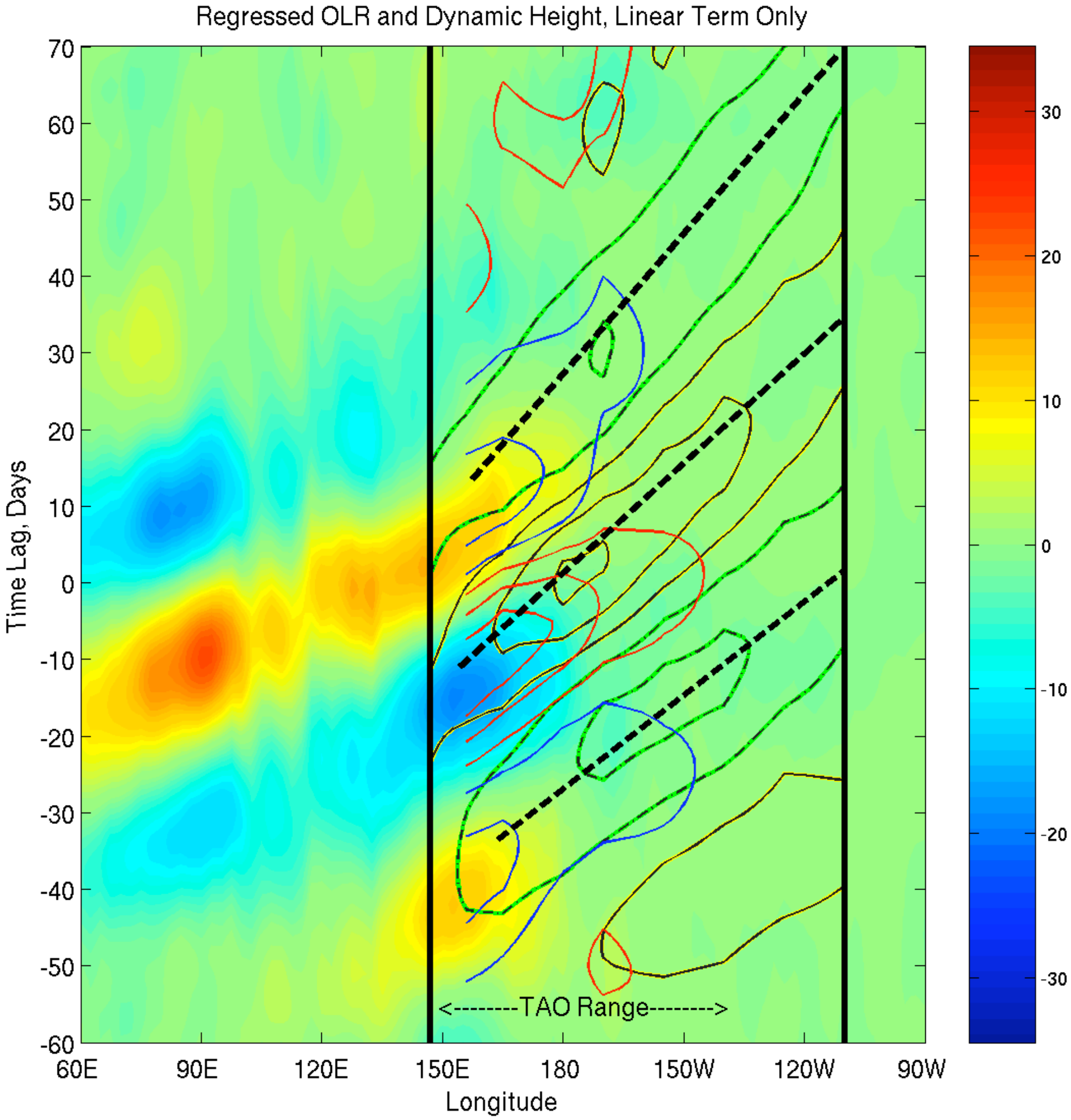

Figure 5 Fully linear regression composite of OLR, TAO wind stress, and dynamic height, including only term 3 in equation 1, contoured as in Figure 4. The wind stress contour interval is 3 m^2s^{-2}, with minimum contours at +/- 1.5 m^2s^{-2}. Dynamic height contours are drawn every 1 cm, with the zero line omitted. Quantities are averaged in latitude as in Fig. 4.

Figure 6

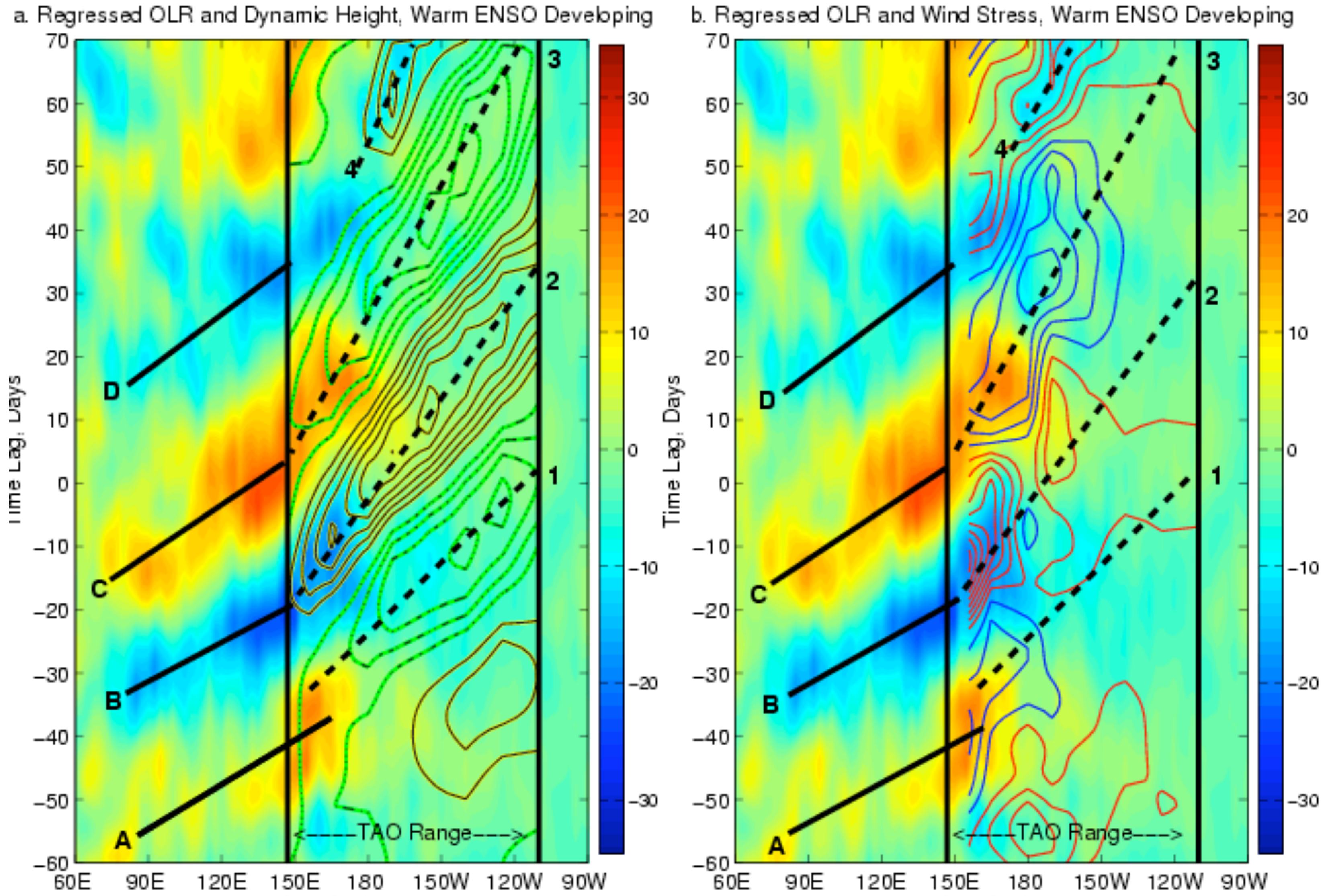

Figure 6 Longitude-time lag regression composite of OLR, the zonal component of the TAO wind stress, and dynamic height, plotted as described in Figures 5, except that panel a shows regressed OLR and dynamic height and panel b shows OLR and wind stress. This composite is based on an index of Kelvin wave dynamic height at the equator and the dateline, and includes terms in equation 1 with subscripts 3-12. Solid lines labeled a-d track active and suppressed phases of the MJO, while dashed trajectory lines (labeled 1-4) track Kelvin wave dynamic height anomalies. Quantities are averaged in latitude as in Fig. 4.

Figure 7

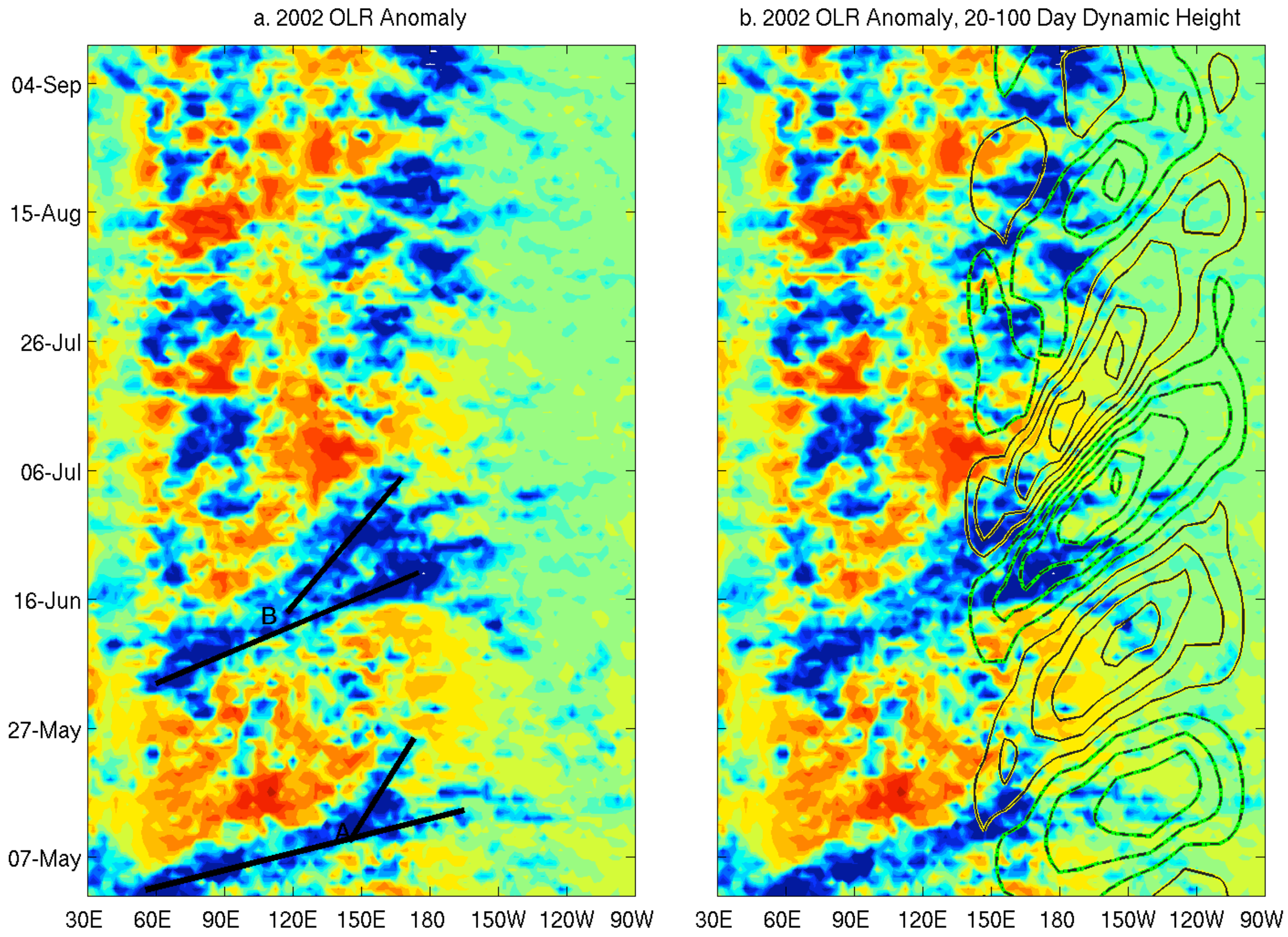

Figure 7 OLR and dynamic height anomalies during 2002. Panel a shows OLR only, for clarity. Dynamic height anomalies were band pass filtered for the 20-100 day periods, and negative anomalies are dashed and positive are solid. Contours are every 2 cm, except that the zero contour is removed. Trajectories of prominent eastward moving negative OLR anomalies are traced by heavy solid lines in panel a.

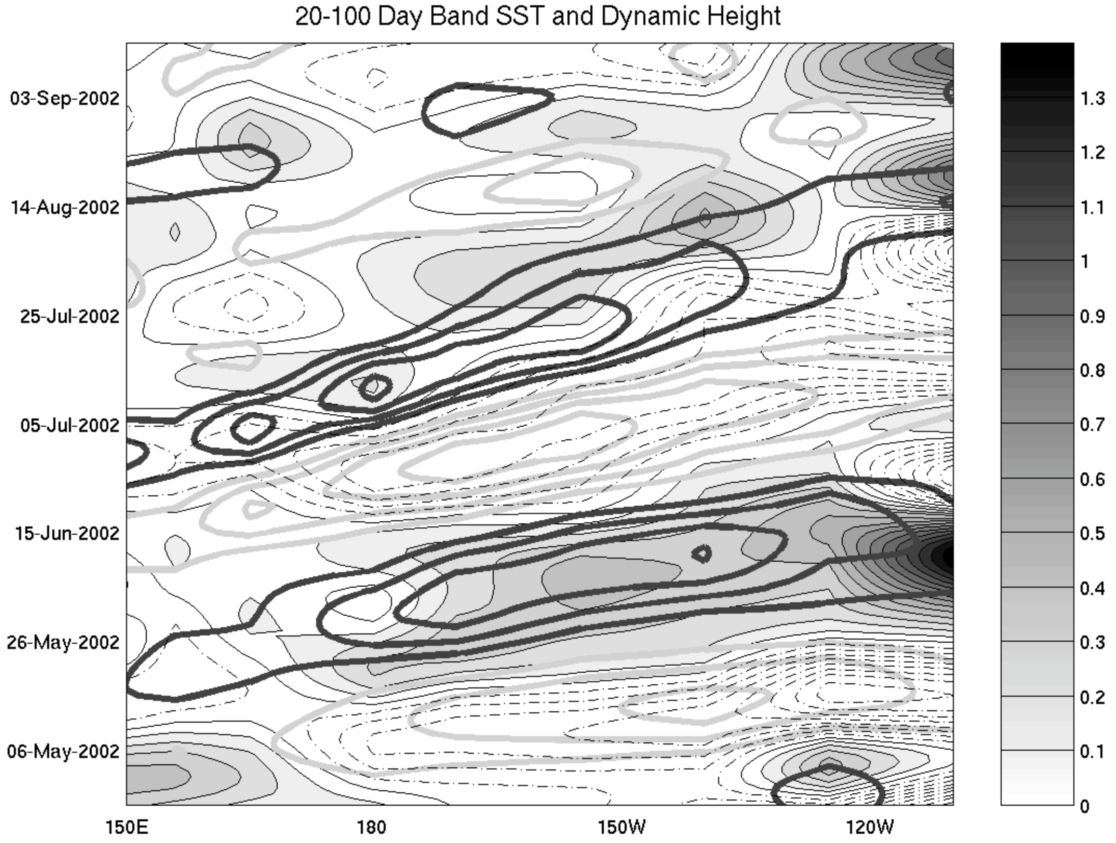

Figure 8 20-100 day band pass filtered dynamic height and SST on the equator preceding the 2002 El Niño, for the same period shown in Figures 2 and 7. Thick gray contours represent negative dynamic height anomalies and black positive anomalies. Dashed contours represent negative SST anomalies and shading represents positive SST anomalies. Contour intervals are 2cm (with the zero contour omitted) and 0.25°C.

Figure 9

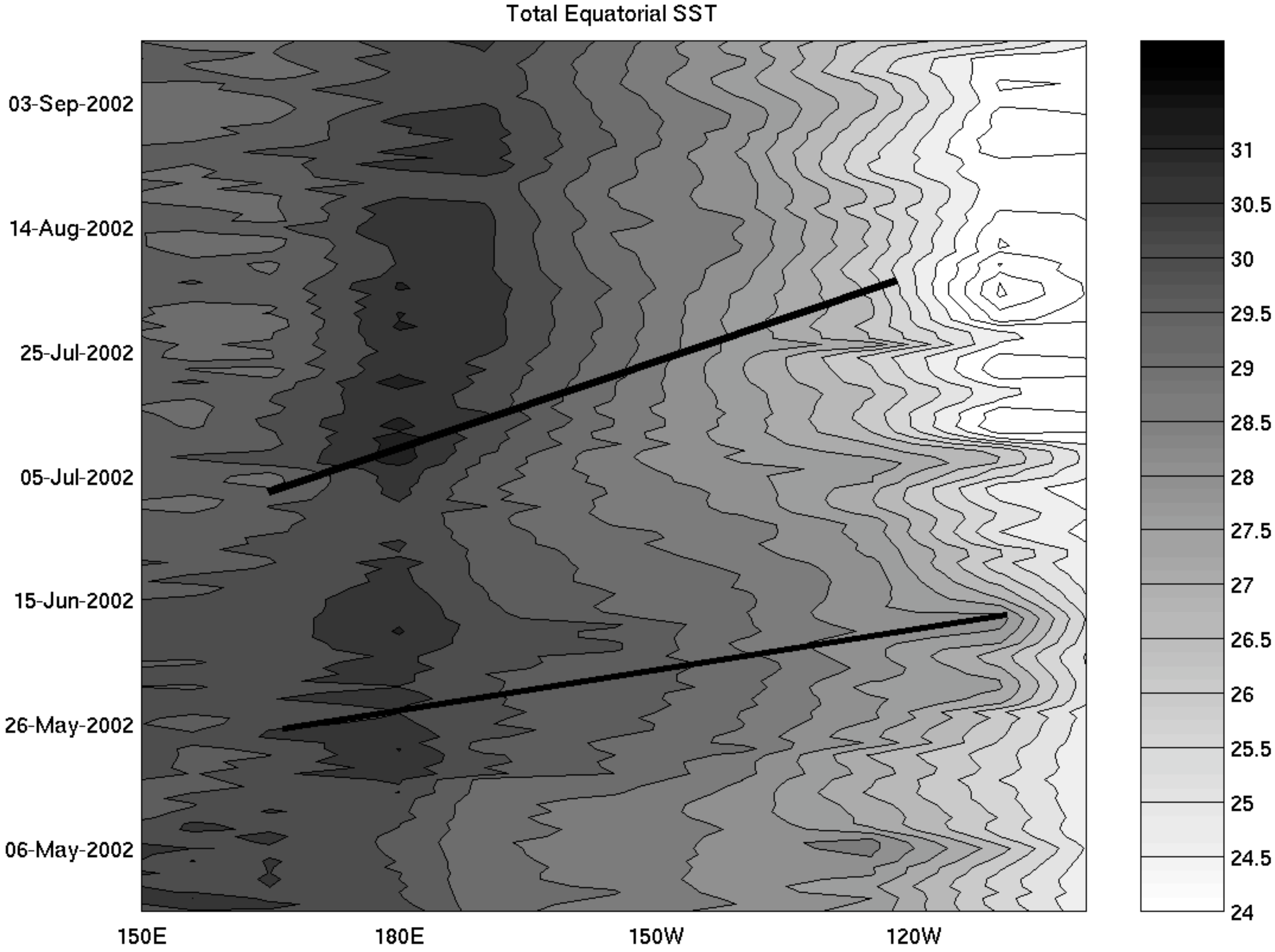

Figure 9 Total SST on the equator for the development period of the 2002 El Niño. Heavy solid lines approximate the trajectories of the dynamic height anomalies of the two downwelling Kelvin waves seen in the first half of Figure 1 and in Figures 2, 7, and 9. Contour interval is 0.5°C.

Figure 10

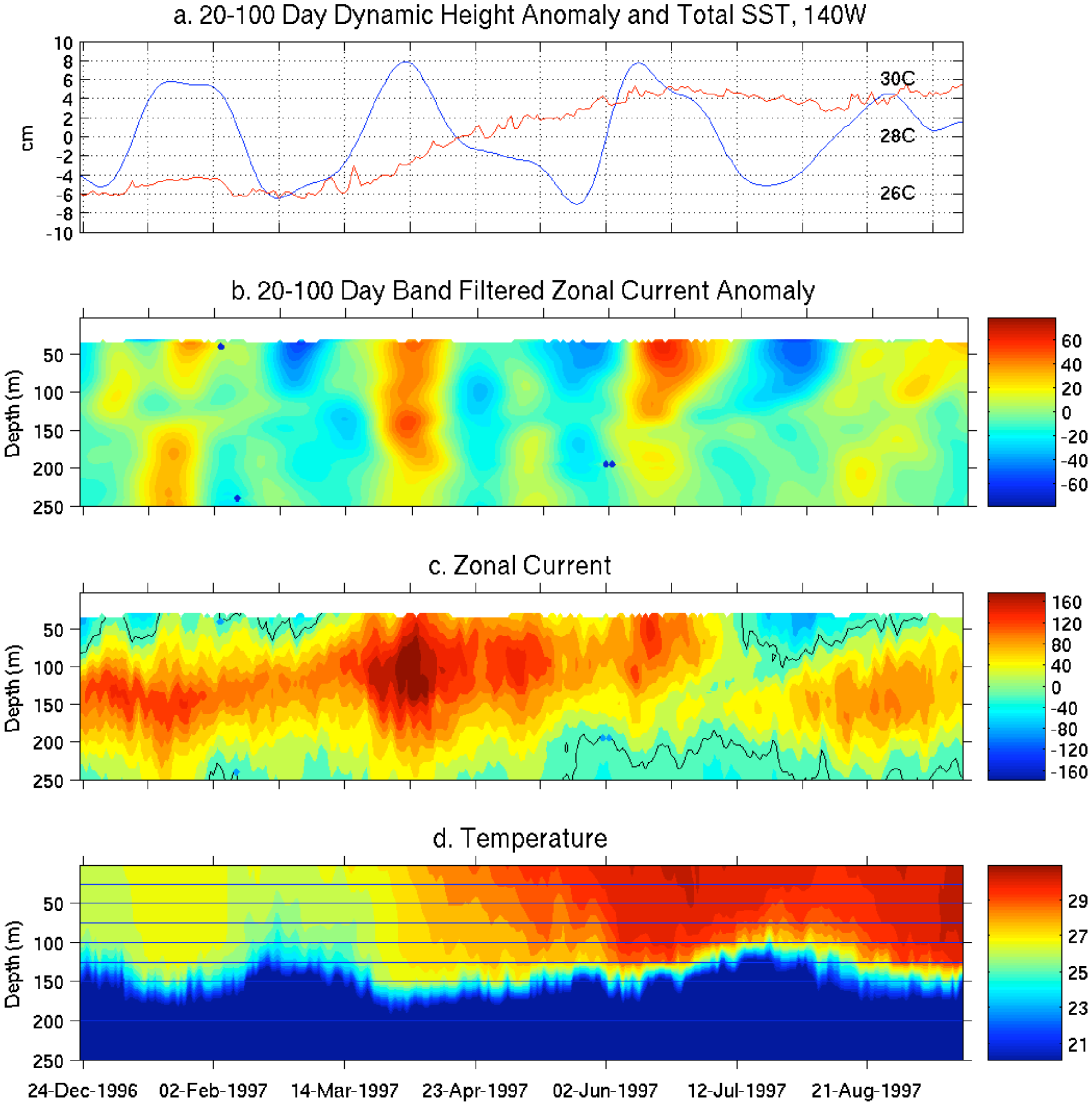

Figure 10 As in Figure 2, except for 23 December 1996 through 20 September 1997.

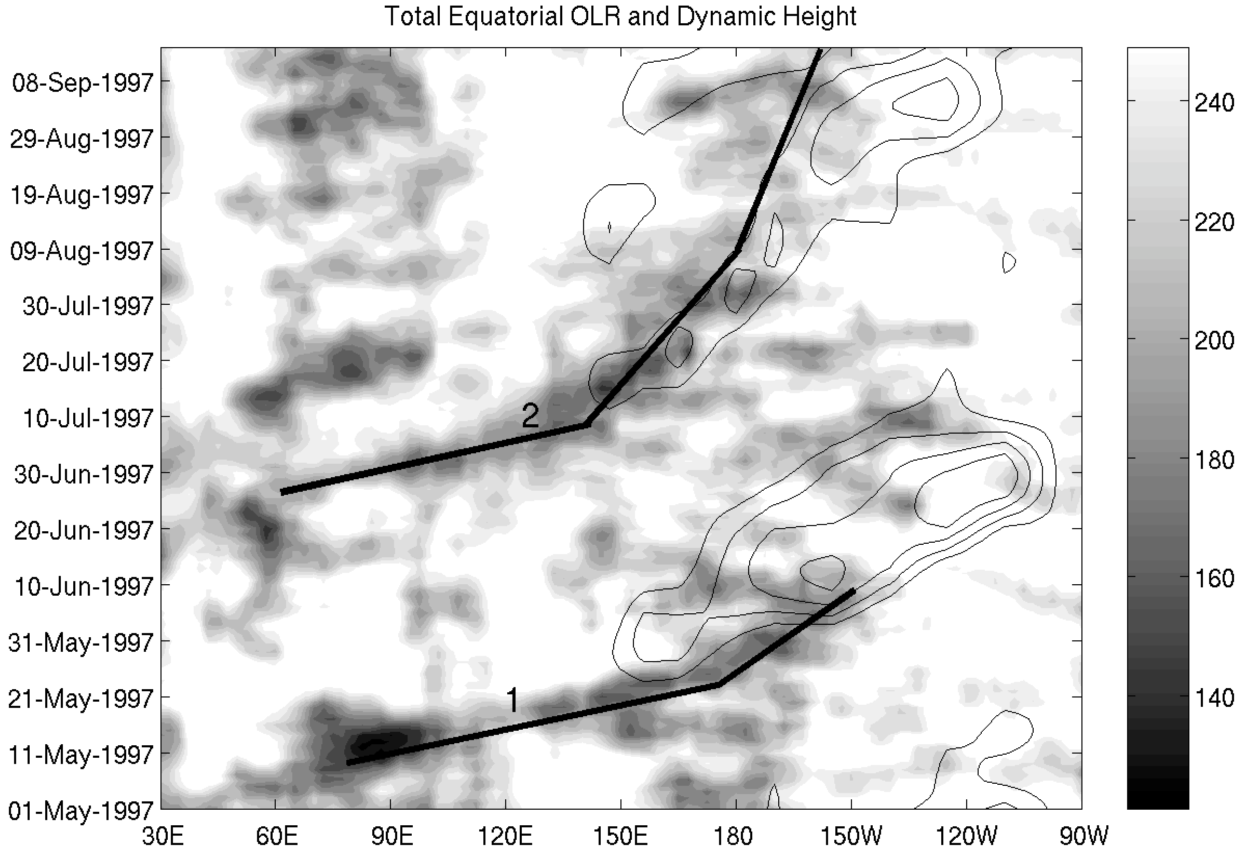

Figure 11 Total OLR (shaded) and 20-100 day band dynamic height (both on the equator). Contour interval for the dynamic height is 1 cm, and negative contours are not plotted. White lines approximate trajectories of strong negative OLR anomalies.

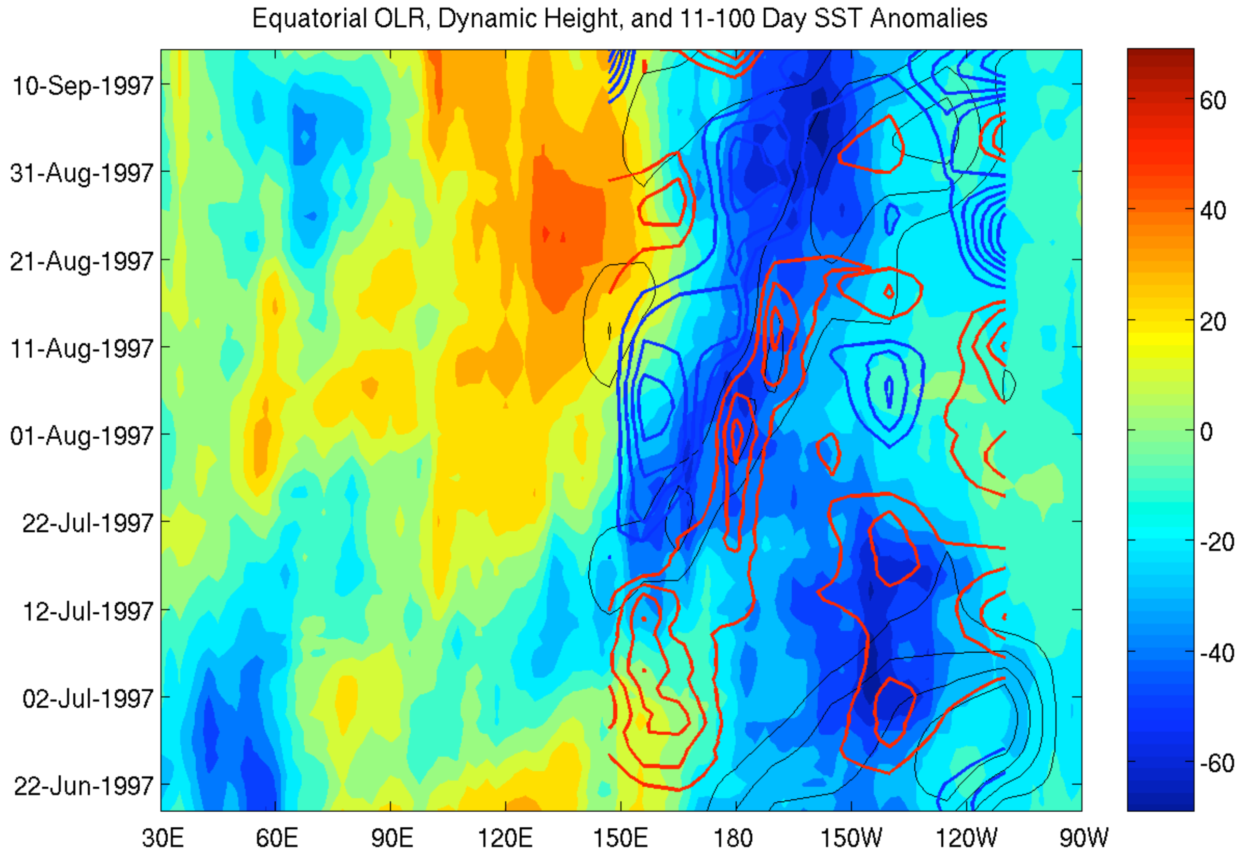

Figure 12 OLR anomaly (shading), SST (positive shown in red contours, negative in blue), and positive dynamic height contours (thin black contours), for the event labeled trajectory 2 in Figure 12. SST contours are every 0.1°C, and the zero contour is omitted. All quantities are plotted on the equator.

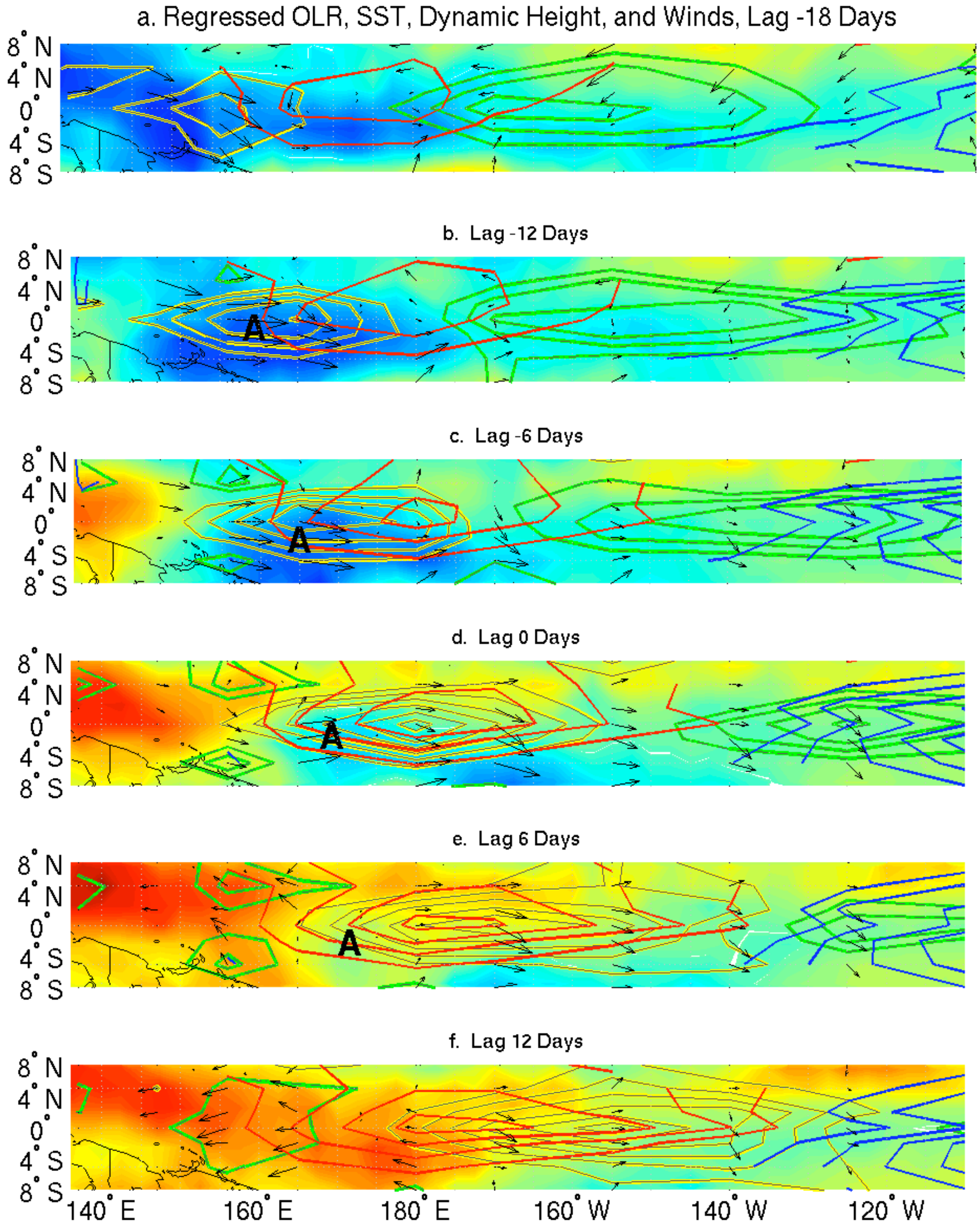

Figure 13 Maps of regressed OLR anomaly (shading), dynamic height (green contours in integer cm, contours beginning at 2 cm), positive SST anomalies (red contours, at intervals of 0.25°C), and TAO surface winds (vectors) for lags of –24 to 6 days wind an interval of 6 days. The regressed SST data includes the ENSO modulation terms (1 and 2 in equation 1) in addition to the intraseasonal terms 3-12 that are included in the dynamic height and wind composites. The largest vectors are around 3 ms^{-1}.